UNIVERSITÀ DEGLI STUDI DI PADOVA

Dipartimento di Fisica e Astronomia "Galileo Galilei"

Master Degree in Physics

Final Dissertation

Modeling of the GERDA data after the upgrade

Thesis supervisor

Prof. Riccardo Brugnera

Thesis co-supervisor

Dr. Katharina von Sturm

Dr. Luigi Pertoldi

Candidate

Michele Morella

Academic Year 2019/2020

Contents

Introduction

The discovery of neutrinos oscillation proved that neutrinos are massive particles. This is the first ever direct evidence of physics beyond the Standard Model, because in this framework neutrinos are inserted as massless particles. But still we do not have information about their absolute mass scale, the mass-generating mechanism, CP-tranformation properties and whether they are Dirac or Majorana particles. Being neutral particles, neutrinos could also be identical to their own antiparticles making them the only fundamental fermions to be Majorana particles. In order to solve some of the problems addressed before the neutrinoless double beta decay ($0\nu\beta\beta$), an extremely rare nuclear decay that has not been observed yet, is currently hunted in many experiments around the world. If this SM-forbidden process will ever be observed then the total lepton number violation and the Majorana nature of neutrinos will be demonstrated, regardless of the underlying mechanism allowing such a process. These two are the base assumptions for many theories beyond the SM trying to explain the cosmological observation of the imbalance between matter and antimatter: today we know that the Universe is filled with matter and no antimatter at all, even though according to our present knowledge we would expect a symmetric situation. These means that, during the evolution of the Universe, a matter-creating process took place creating the Universe as we see it today. In $0\nu\beta\beta$ only two electrons and no antineutrinos are emitted after two simultaneous β-decay: this is indeed a process where only matter is present in the final state.
One of the candidate isotopes that could undergo $0\nu\beta\beta$ decay is ^{76}Ge. Germanium is already used to build high-purity particle detectors with excellent energy resolution and the idea of incorporating the source into the detector medium makes the potential of this discovery channel immediately evident. Up to now no evidence for this decay have been reported, only limits on its half-life. GERDA was an experiment operating ^{76}Ge at Laboratori Nazionali del Gran Sasso between 2008 and 2019. The core of the experiment was an array of forty High Purity Ge (HPGe) detectors submerged bare into Liquid Argon, providing passive and active shielding thanks to its scintillation properties. Thanks to various background mitigation techniques, GERDA has been operating in background-free conditions for the largest part of its collected exposure. This achievement has successfully demonstrated the maturity of the germanium technology as the base of a next-generation, tonne-scale experiment, which is currently being prepared by the LEGEND collaboration. Since the signal of this process is hypothetical and possibly faint, the search for a signal becomes a quest to reduce the background events rate. This is done during the design and construction phase by not exposing detectors to background sources, passively and actively shielding them, screening materials placed in the vicinity of the detectors before deployment; still a residual background is observed. In 2018 many upgrades have been performed on the experimental apparatus of GERDA. In this thesis a model of the full-range energy spectrum acquired by the germanium detectors is studied. All the analysis is done

using Bayesian statistics approach (parameter estimation, hypothesis testing, etc.). The spectrum is modeled by means of Monte Carlo simulations reproducing possible radioactive isotopes, coming from U and Th chains or from cosmogenic activation, distributed in different components of the apparatus (cables, LAr, etc.) that can give significant contribution. The parameters of interest (isotopes activities, two neutrino beta decay's half life) are then estimated from the data using Markov Chain Monte Carlo algorithms while direct screening measurements of the apparatus' components (if available) are introduced as prior distributions in the analysis. For very high statistics gamma decay lines (^{40}K and ^{42}K) a detector by detector study of the number of registered counts is performed in order to get a more accurate and reliable assessment of the activities of the isotope generating these events; then they are inserted as prior distributions in the full-range fit. From this analysis it will be possible to understand the origin of the collected events, make a precise measurement of the half-life of the allowed two neutrino decay mode and could also give information about the purity of the materials for future experiments' strategies. Moreover this study will help a lot the search for the neutrinoless double-beta decay in the region around $Q_{\beta\beta}$.
In Chapter 1, after a brief introduction about neutrinos discovery and properties, the two neutrino and the neutrinoless double beta decay modes are presented. Chapter 2 describes the experimental apparatus of GERDA during PhaseII and the further improvement that have been made after the upgrade during PhaseII$^+$. Chapter 3 deals with some basic concepts of Bayesian statistics and inference and the algorithms to implement them. In Chapter 4 after a presentation of the dataset and the MC simulations used, the potassium tracking and the full range fit analysis are explained.

Chapter 1

Double Beta Decay

1.1 Neutrinos and Oscillation

The existence of neutrinos was hypothesized by W. Pauli in 1930 in order to account for the continuous energy spectrum of electrons emitted in β-decay and for the angular momentum violation occurring in the same phenomenon. The solution was to consider a three body process

$$(A, Z) \rightarrow (A, Z+1) + e^{-} + \nu$$

in which a very light (with a mass of the order of the electron one or less), electrically neutral and spin 1/2 particle was also emitted. The first model explaining this decay was proposed by E. Fermi [1] and consisted in a four fermion contact interaction that well reproduced also other scattering and decay phenomena mediated by weak interactions. After the discovery that weak interactions violates parity in the famous experiment carried on by madame Wu [2] and the measurement of the neutrinos helicity [3] (which demonstrated that only left-handed neutrinos and right-handed antineutrinos join weak interactions) the so called $V - A$ theory of weak interactions was formulated, a chiral theory in which neutrinos were introduced as massless neutral particles with 1/2 spin. No experiment was able to measure neutrinos' mass, only upper limits of the order of the eV were estimated [4] [5] [6].

The most complete model describing fundamentals particles' properties and interactions (including neutrinos) is the Standard Model. Matter particles are divided into leptons and quarks (the latter are the only one feeling the strong interactions); according also to previous information, neutrinos are leptons with no electric charge, they come into three flavors (group of particles with same quantum numbers but different mass and lifetime), are assumed to be massless and interact only through weak interactions. Quarks and leptons are embedded in the theory in left-handed chirality doublets and right-handed chirality singlets (as well as their corresponding antiparticles but with opposite chirality):

$$\begin{pmatrix} \nu_e \\ e \end{pmatrix}_L \ , \ e_R \qquad \begin{pmatrix} u \\ d \end{pmatrix}_L \ , \ u_R \ , \ d_R$$

In order to write a mass term for all the SM particles, both chirality states for each particle have to be included; indeed, it can be shown that for a given particle described by a spinor Ψ:

$$\mathcal{L}_{mass} = m\overline{\Psi}\Psi = m(\overline{\Psi}_L\Psi_R + \overline{\Psi}_R\Psi_L). \tag{1.1}$$

and in the SM mass terms arise thanks to the coupling of the Higgs field with the matter particles after spontaneous symmetry breaking.

Although neutrinos were supposed to be massless, two experiments proved this assumption to be wrong. In 1993 the Super-Kamiokande collaboration [7] measured a deficit of the muon neutrinos' flux produced in the interaction of cosmic rays with the atmosphere with respect to the expectations. The data were compatible with the hypothesis that ν_μ oscillated (i.e. changed flavor) into ν_τ while propagating, before being detected. In 2001, in order to solve the so called solar neutrino problem (a deficit in the expected electron neutrino flux produced in the pp chain inside the Sun), the SNO collaboration [8] was able to measure fluxes of all neutrinos' flavor and their sum was in agreement with the expected value of a purely electronic neutrinos flux. In both cases the property of neutrinos to change flavor while propagating in vacuum (atmospheric neutrinos, ν_μ-air interaction is negligible) or in matter (solar neutrinos, ν_e-electron interaction inside the Sun) was established. As a consequence individual flavor lepton number is no more conserved (like in the SM), but the total lepton number is still preserved [1].
Neutrinos oscillation can be explained by assuming a mixing between neutrinos' flavor states and mass states, just like what happens in the quarks sector: the particles joining the interaction (flavor states) are different from the physical ones (mass states) but these two bases are connected through a rotation matrix. In general a neutrino of flavor $\alpha = e, \mu, \tau$ can be thought as superposition of mass states $i = 1, 2, 3$:

$$|\nu_\alpha\rangle = \sum_i U_{\alpha i} \, |\nu_i\rangle \, . \tag{1.2}$$

If we assume that in a given weak interaction a neutrino with flavor α has been produced, we can compute the probability that the flavor will change to β during propagation after a distance L (vacuum is assumed for simplicity):

$$\begin{aligned} P_{\alpha\beta} = |\langle\nu_\beta|\nu_\alpha\rangle|^2 = \delta_{\alpha\beta} - 4\sum_{i<j} \mathrm{Re}\{U^*_{\beta i} U_{\alpha i} U_{\beta j} U^*_{\alpha j}\} \sin^2\left(\frac{\Delta m^2_{ij}\, L}{4E}\right) \\ \pm 2\sum_{ij} \mathrm{Im}\{U^*_{\beta i} U_{\alpha i} U_{\beta j} U^*_{\alpha j}\} \sin\left(\frac{\Delta m^2_{ij}\, L}{2E}\right). \end{aligned} \tag{1.3}$$

Because the transition probability is proportional to the term Δm^2_{ij}, it is non trivial only if the mass eigenvalues are different from zero and different among them (in order to have oscillation in three flavors this condition must be fulfilled by at least two of them). Therefore the previous oscillation experiments proved that neutrinos do have mass. Given three families of leptons and thus three mass eigenvalues, only two square mass differences are independent and can be measured from oscillation experiment. From solar neutrinos studies it has been possible to remove the degeneracy on Δm^2_{12} and so $m_2 > m_1$, but still there are no information about Δm^2_{23} sign leading to two different scenarios as represented in Figure 1.1.
The mixing matrix is called PMNS matrix, in honor of the physicists that proposed this model (Pontecorvo-Maki-Nakagawa-Sakata) and it can be factorized (for three flavors

[1] Lepton number (and also barionic number) conservation is just a consequence of an accidental global symmetry of the Standard Model, that instead is based upon local gauge symmetries (the true symmetries to be preserved). Therefore there are no reasons nor theoretical motivations for even total lepton number to be conserved.

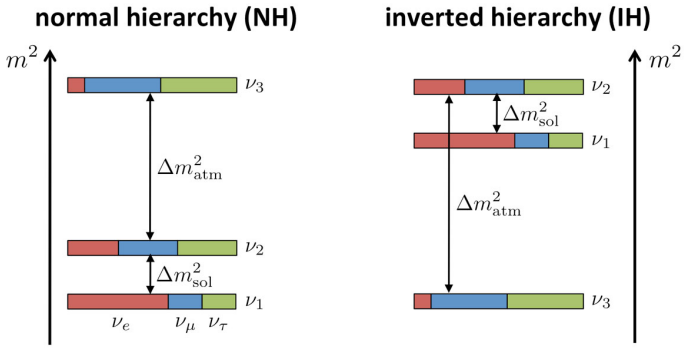

Figure 1.1: Possible neutrinos hierarchy according to the sign of Δm^2_{23}. Two configurations are possible: $\nu_3 > \nu_2 > \nu_1$ (normal hierarchy) and $\nu_2 > \nu_1 > \nu_3$ (inverted hierarchy).

mixing) in 3 rotation angles and 1+2 complex phases:

$$U_{PMNS} \equiv \begin{pmatrix} 1 & 0 & 0 \\ 0 & c_{23} & s_{23} \\ 0 & -s_{23} & c_{23} \end{pmatrix} \begin{pmatrix} c_{13} & 0 & s_{13}e^{-i\delta} \\ 0 & 1 & 0 \\ -s_{13}e^{i\delta} & 0 & c_{13} \end{pmatrix} \begin{pmatrix} c_{12} & s_{12} & 0 \\ -s_{12} & c_{12} & 0 \\ 0 & 0 & 1 \end{pmatrix} \begin{pmatrix} 1 & 0 & 0 \\ 0 & e^{i\gamma_1} & 0 \\ 0 & 0 & e^{i\gamma_2} \end{pmatrix} \tag{1.4}$$

The last two complex phases have to be included if neutrinos are Majorana particles, i.e. they are the same as their antiparticle; on the other hand, if neutrinos are Dirac particles then they are different from their antiparticles and behave excatly like all other fundamental fermions and the two additional phases vanishes.

Neutrinos mass and nature are the only direct evidences for new physics beyond the Standard Model because these effects cannot be explained within this theory: as we have seen before, since neutrinos do not have right-handed chirality states, they do not acquire mass after SSB and stay massless. Yet, from oscillation experiments, we can gain information on square mass differences but no clue about absolute mass scale and neutrinos nature (Majorana phases cancel). Therefore other processes are needed in order to shed light on these neutrinos properties such as the (forbidden) neutrinoless double beta decay.

1.2 Two Neutrino Double Beta Decay

The possibility that a nucleus could undergo double beta decay was first proposed by M. Goeppert-Mayer in 1935 [9]. This decay is a second-order weak process and consists in the decay of two neutrons (protons) into two protons (neutrons) with the emission of lepton/antilepton pairs (see Figure 1.2a):

$$\beta^-\beta^- : \quad N(A,Z) \to N(A,Z+2) + 2e^- + 2\overline{\nu}_e \tag{1.5}$$

$$\beta^+\beta^+ : \quad N(A,Z) \to N(A,Z-2) + 2e^+ + 2\nu_e \tag{1.6}$$

The $Q_{\beta\beta}$ value is smaller in the case of $\beta^+\beta^+$. Consequently the process has a smaller probability compared with $\beta^-\beta^-$ decay due to a smaller phase space, and experimentally it is much more challenging to observe. Double beta decay is allowed if a single beta decay is strongly suppressed or energetically forbidden and this is the case of some even-even nuclei; in fact, the final state would be an odd-odd nucleus and it could have a lower binding energy than the decaying nucleus as shown in Figure 1.2b for ^{76}Ge (this can be

explained as the effect of the pairing term in the semi-empirical mass formula). If both single and double beta decay modes are allowed then the latter would be impossible to observe because β-decay would have a much shorter lifetime than 2β-decay.

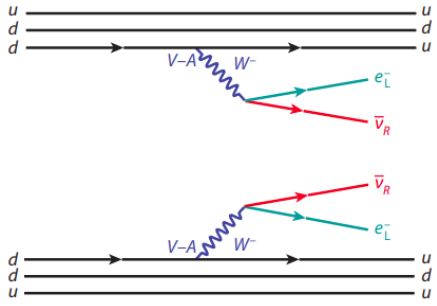

(a) Feynman diagram of $2\nu\beta\beta^-$ decay. Picture from [10]

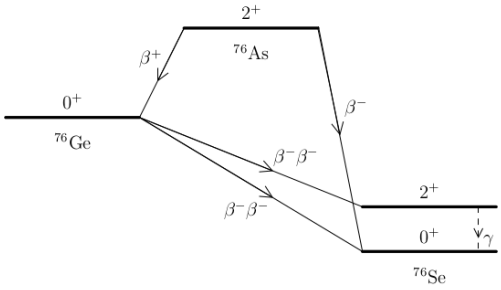

(b) The decay of ^{76}Ge to ^{76}As is energetically not allowed because final state has a greater energy than initial one; ^{76}Ge can only decay through 2β to (ground state or excited state) of ^{76}Se. Picture from [11]

Figure 1.2

The experimental signature of this decay is the detection in coincidence of the two emitted electrons and their energy has a continuous spectrum because part of the energy is carried away by neutrinos (that are not detected). $2\nu\beta\beta$ between ground state of initial and final nuclei has been observed in about ten different isotopes with an half-life greater than the age of the Universe ($10^{18} \div 10^{21}\ yr$); the one we are interested in is ^{76}Ge since is the one used in the GERDA experiment [12] and its measured half-life is $T^{2\nu}_{1/2} = (1.926 \pm 0.094) \times 10^{21}\ yr$ [13]. The half-life for $2\nu\beta\beta$ can be factorized, in a good approximation, as

$$\left[T^{2\nu}_{1/2}\right]^{-1} = G_{2\nu}|M_{2\nu}|^2. \tag{1.7}$$

$G_{2\nu}$ is the phase space factor, it is computed by integrating over all the possible final states involving the emitted leptons and it can be computed quite accurately as described in [14]; $M_{2\nu}$ is the nuclear matrix element and it contains information about the physics of the nuclear transition and its computation is quite challenging because different models give different results.

1.3 Neutrinoless Double Beta Decay

Neutrinoless double beta decay ($0\nu\beta\beta$), differently from $2\nu\beta\beta$, is not allowed in SM because it violates total lepton number by two units. It requires neutrinos to be Majorana particles[2], and it was first suggested by W.H. Furry [15] while trying to explain the phenomenon predicted by M. Goepper-Meyer using Majorana's theory.
The consequence of this process is the absence of neutrinos in the final state:

$$\beta^-\beta^- : \quad N(A,Z) \rightarrow N(A,Z+2) + 2e^- \tag{1.8}$$
$$\beta^+\beta^+ : \quad N(A,Z) \rightarrow N(A,Z-2) + 2e^+ \tag{1.9}$$

[2]Being electrically neutral, neutrinos are the only candidates among fundamental fermions to have such a feature (as a consequence of the invariance under charge conjugation symmetry)

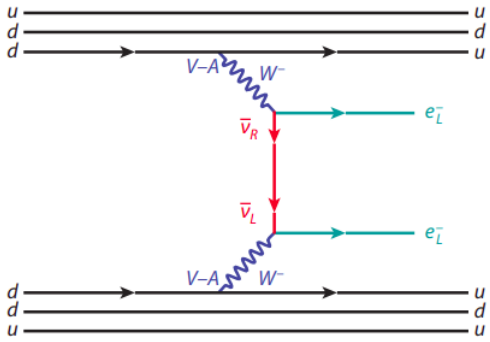

(a) $0\nu\beta\beta$ via light majorana neutrino exchange; in the final state we only have electrons and the total lepton number is violated by two units. Picture from [10]

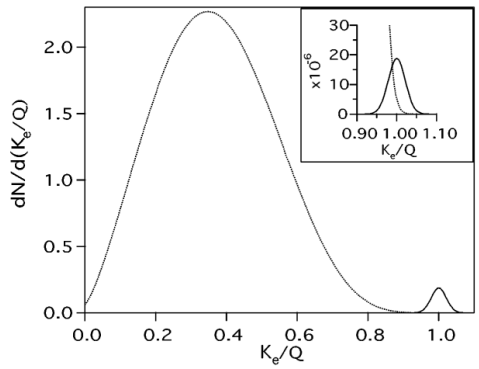

(b) Sum of electrons kinetic energies K_e in units of the Q value. Dotted line: $2\nu\beta\beta$; solid line: $0\nu\beta\beta$. Picture from [16]

Figure 1.3: $0\nu\beta\beta$ Feynman diagram and electrons energies spectrum in both $2\nu\beta\beta$ and $0\nu\beta\beta$

In this way the decay becomes a two body process (seeing the two final state electron as a single particle) and the sum of electrons energy is fixed: thus the experimental signature of this process is no more a distribution but a single peak at an energy equal to the Q value of the reaction (see Figure 1.3b).
There are more than one mechanism that can explain this decay; the simplest one (the so called standard interpretation) requires the exchange of a light Majorana neutrino (see Figure 1.3a) but many other mechanisms are possible like for example heavy right-handed neutrinos or Majorons (non-standard interpretation); actually, all these models are not mutually exclusive and can contribute at the same time.

The half-life for $0\nu\beta\beta$ can be factorized as follow:

$$\left[T^{0\nu}_{1/2}\right]^{-1} = G_{0\nu}|M_{0\nu}|^2|\langle\eta\rangle|^2. \tag{1.10}$$

where $|\langle\eta\rangle|^2$ is a new term that takes into account the mechanism mediating the decay. In the standard interpretation

$$\langle\eta\rangle = \frac{\langle m_{\beta\beta}\rangle}{m_e^2} = \sum_{i=1}^{3}\frac{U_{1i}^2 m_i}{m_e^2} = \frac{c_{12}^2c_{13}^2m_1 + s_{12}^2c_{13}^2e^{i\gamma_1}m_2 + s_{13}^2e^{i\gamma_2}m_3}{m_e^2}. \tag{1.11}$$

$\langle m_{\beta\beta}\rangle$ is called effective Majorana mass and is a sum of the neutrinos mass eigenvalues weighted with the first row of the PMNS matrix; it's worth mentioning that this observable depends on the Majorana phases and since the matrix elements are just squared (and are complex numbers), cancellations among the three terms are possible. Experimental lower bounds on $T^{0\nu}_{1/2}$ for some experiments are reported in Table 1.1 as well as limits on the effective Majorana mass $\langle m_{\beta\beta}\rangle$ in the hypothesis of light Majorana neutrinos exchange; interval on $\langle m_{\beta\beta}\rangle$ are due to different models exploited to compute the corresponding nuclear matrix element for a given isotope.

If this decay will ever be observed many information could be obtained: first of all such a measurement will prove the non conservation of total lepton number and the Majorana nature of neutrinos; these two are the base ingredients for many models trying to explain the asymmetry matter/antimatter in our Universe; by measuring $T^{0\nu}_{1/2}$ and knowing the phase

Experiment	Isotope	Exposure (kg·yr)	$T^{0\nu}_{1/2}$ (10^{25} yr)	$\langle m_{\beta\beta}\rangle$ (meV)
GERDA [17]	^{76}Ge	127.2	18	80-182
MAJORANA [18]		26	2.7	200-430
CUORICINO [19]		19.8	0.28	300-710
CUORE-0 [20]	^{130}Te	9.8	0.24	270-760
CUORE [21]		372.5	3.2	75-350
EXO-200 [22]	^{136}Xe	234.1	3.5	93-296
KAMLAND-ZEN [23]		594	10.7	61-165

Table 1.1: Experimental bounds on $T^{0\nu}_{1/2}$ and $\langle m_{\beta\beta}\rangle$ of some $0\nu\beta\beta$ experiments running on ^{76}Ge, ^{130}Te, ^{136}Xe. A value of $g_A \simeq 1.27$ is used.

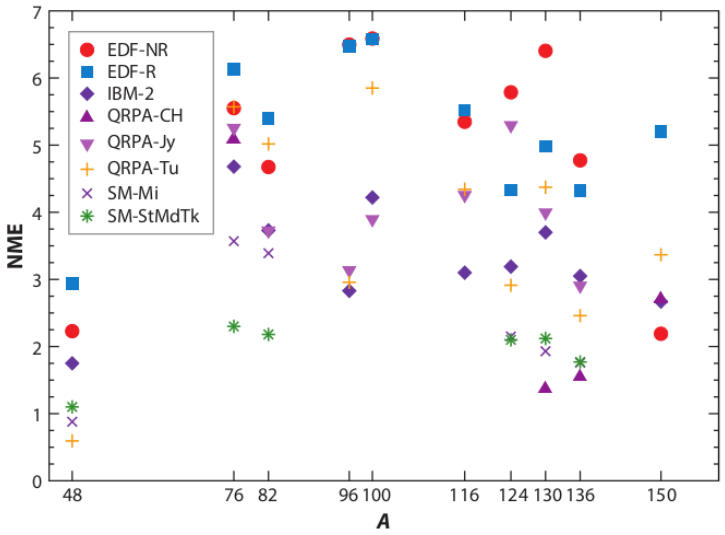

Figure 1.4: Nuclear matrix elements for $0\nu\beta\beta$ candidate isotopes; all the values are calculated with g_A fixed at the 1.27. Picture from [24]

space term and the nuclear matrix element is possible to compute the effective Majorana mass term (or the more general term $\langle\eta\rangle$, that in any case is linked to neutrinos' masses). The first two results are model-independent but the computation of the mass parameter strongly depends on the other terms in 1.10. As mentioned in the previous paragraph, the phase space factor can be computed accurately, but the two main sources of uncertainties are the choice of the nuclear model to exploit for calculation and the value of the axial coupling constant g_A. As we can see in Figure 1.4, each model makes a different prediction for the same isotope (there is a difference of the order of a factor two or three).
For ground state to ground state transition, it is possible to perform the same approximation of a simple β-decay and the nuclear matrix element can be written as the sum of Gamow-Teller and Fermi transitions:

$$|M_{0\nu}| = M_{GT} - \frac{g_V^2}{g_A^2} M_F \tag{1.12}$$

and thus $\left[T_{1/2}^{0\nu}\right]^{-1} \propto g_A^4$. Given this strong dependence, uncertainties on g_A values can propagate on $m_{\beta\beta}$. Usually this value is "quenched" with respect to the expected one in the free-nucleon approximation in order to fit the experimental results of $2\nu\beta\beta$, but nothing prevents g_A to have a different value in the $0\nu\beta\beta$ process.

Chapter 2

The GERDA experiment

The GERDA experiment (GERmanium Detector Array) is devoted to the search of $0\nu\beta\beta$ in ^{76}Ge using High Purity Germanium (HPGe) detectors. Since isotopic fraction f_{76} of ^{76}Ge in natural germanium is about 7.8%, the diodes are made of enriched material reaching a fraction of 86% or higher, thus acting also as source of $0\nu\beta\beta$ and increasing the detection efficiency of the experiment. Another advantage of operating enriched HPGe is the great energy resolution of 0.2% at $Q_{\beta\beta} = 2039\,keV$ whereas disadvantages are the low end point (background falls with increasing energy) and the cost to deploy larger mass to perform ton-scale experiment with respect to liquid or gas based experiments.
GERDA has been built underground at 3500 m w.e. (water equivalent) depth at the INFN Laboratori Nazionali del Gran Sasso (LNGS). A first data collection, named Phase I, has been running between November 2011 and June 2013 with 8 semi-coaxial detectors inherited from the Heidelberg-Moskow (HdM) [25] and IGEX [26] experiments and 5 Broad Energy Germanium (BEGe) detectors for a total mass of 17.7 and 3.7 kg, respectively. The total exposure of Phase I is 21.6 kg·yr and a Background Index (BI) of $1.1 \cdot 10^{-2}$ counts/(keV·kg·yr) was achieved. No excess or signal were found and the experimental limit on $0\nu\beta\beta$ half-life at 90% C.L. $T^{0\nu}_{1/2} > 2.1 \cdot 10^{25}\,yr$ was established [27].
Phase II started in December 2015 after a major upgrade of the apparatus [28], such as the addition of 30 new BEGe detectors and a new veto system based on LAr scintillation light detection, in order to improve the BI by one order of magnitude remaining in the background free regime[1] for the entire data taking period where sensitivity scales linearly with exposure. In this new configuration, GERDA reached a BI of about $6 \cdot 10^{-4}$ counts/(keV·kg·yr) and a lower limit of $0.9 \cdot 10^{26}$ yr (90% C.L.) by April 2018 [29].
At this point a new upgrade was performed in which five inverted-coaxial germanium detectors were added for a total mass of 9.6 kg. This last part of the data taking (named Phase II$^+$) lasted until November 2019. So during the entire Phase II a final exposure of 103.7 kg·yr of data was collected. No events were found within $\pm 2\sigma$ around $Q_{\beta\beta}$ and a final lower limit (equal to the sensitivity) was put of $T^{0\nu}_{1/2} > 1.8 \cdot 10^{26}\,yr$ (90% C.L.) [17].

2.1 GERDA Phase II Experimental Setup

GERDA (see Figure 2.1) exploits germanium detectors arranged in strings within a cryostat filled with 64 m^2 of liquid argon (LAr). One of the main feature of the experiment is

[1] i.e. less than one count is expected in the region of interest $Q_{\beta\beta} \pm 0.5$ FWHM.

Figure 2.1: Artistic representation of the GERDA experiment (detectors not to scale): the germanium detector array (1), the LAr cryostat (2) with its internal copper shield (3), the water tank and the Cherenkov muon veto (4), the GERDA clean room (5) and the lock system (6) [12].

operating bare germanium detectors directly in contact with LAr, resulting in a significant reduction of cladding material (and thus possible background sources) with respect to traditional Ge experiments; also the background induced by cosmic rays is lower than HdM or IGEX due to the lower Z of the shielding material. The cryostat is then surrounded by a tank filled with ultra-pure water, acting as passive shield against external radiation and as cosmic muon veto by measuring Cherenkov light. The detectors are lowered into the LAr using a lock system located in a clean room on top of the water tank. Another muon veto system is placed on top of the clean room.

2.1.1 Germanium Detectors

GERDA Phase II detector array includes seven strings, which carry 40 detectors in total; in this phase three types of detector are present: semi-coaxial (ANG and RG) detectors, BEGe detectors and the semi-coaxial GTF detectors. The detectors of the first two groups are made of germanium enriched in ^{76}Ge, while those of the third group are made of germanium with natural isotopic abundance. All detectors are obtained from high-purity p-type germanium crystals. The n^+ contact, where the external voltage is applied, "wraps around" the detector. It is obtained by deposition of a lithium layer on the surface, which diffuses below the surface until a depth of $\sim$ 1 mm, creating a region where the charge collection is not efficient even if the detector is fully depleted (dead layer). The p^+ electrode, where the signal is read out, is instead fabricated by boron implantation, and the associated dead layer is typically smaller, at the level of hundreds of microns.
Semi-coaxial detectors have a cylindrical shape and a bore-hole is excavated along their axis where the p^+ electrode is implanted. In this configuration relatively large sized detector can be manufactured (2-3 kg) and the enrichment fraction of five ANG and two RG detectors and natural detectors (three GTF) is in the range 85.5-88.3%, for a total mass of 23.2 kg. While the previous detectors where available already in Phase I, during Phase II 30 new diodes of the BEGe type have been added to the setup. The Broad

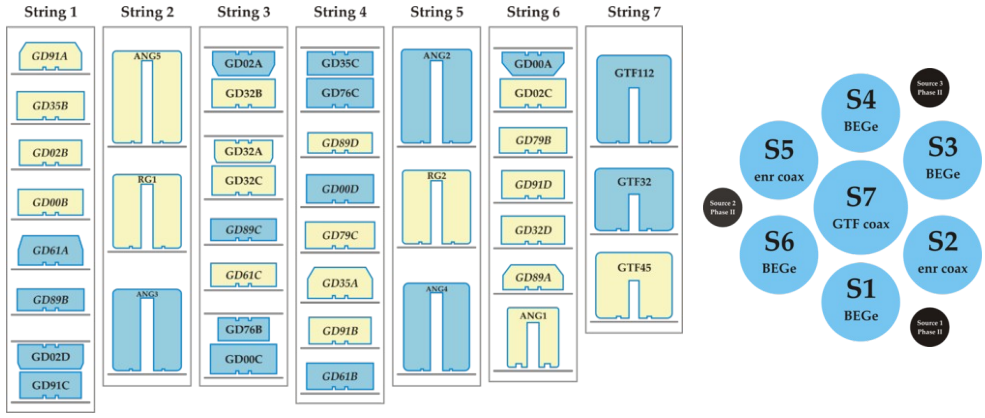

Figure 2.2: Configuration of the 40 detectors of GERDA Phase II in strings (left) and strings position in the detector array and calibration sources (right).

Energy Germanium detector design does not include a bore-hole, therefore the p^+ contact is a small, dot-shaped surface at the center of one of the two detector sides. The absence of a bore-hole makes this kind of detectors harder to electrically deplete, requiring lower impurity concentrations and smaller masses, generally lower than 1 kg. A scheme of the configuration of the aforementioned detectors can be found in Figure 2.2.
Each detector is held by a low-mass and radio-pure silicon plate and three copper bars holding each modulus thus creating a string of detectors (see Figure 2.3a). Both signal and high voltage cables for each detector are connected to silicon plates; the Ge detectors are then read out with custom-produced, cryogenic and low radioactivity preamplifiers called CC3 [30] (scheme of the apparatus in Figure 2.3b). Different cable types are adopted for the signal and HV contact: the HV cables are made of 10 mils Cuflon® , or 3 mils Pyralux® , the signal cables from 3 mils Cuflon® or Pyralux®.

2.1.2 Cryostat and LAr veto system

LAr acts as both cooling medium and shield against the external background penetrating the surrounding water and against the radioactivity of the cryostat itself. After studies of scintillation light detection performed in the low-background facility LArGe [31], an active veto system has been implemented during Phase II, made of 3" PhotoMultipier Tubes (nine on top and seven on bottom of the detector array, see Figure 2.4a) and a curtain of plastic wavelength shifter fibers (Figure 2.4b) around the detector array coupled to a ring of Silicon PhotoMultipliers. The goal of this hybrid system is to reject events depositing energy both in the Ge detectors and in the LAr, such as for example Compton scattered γ-rays from Ra and Th decay chains, cosmic muons decay and $^{42}Ar/^{42}K$ decay inside LAr and thus allowing for a better background discrimination. To improve the light collection efficiency the copper shrouds used in Phase I surrounding each string in the detector array have been replaced by nylon ones (Figure 2.3a), which are transparent and allow light propagation while being a mechanical barrier against the background from ^{42}K naturally presents in LAr, which undergo β-decay and can mimic $0\nu\beta\beta$ at $Q_{\beta\beta}$ [32]. The electric field generated by the HV cables once shielded by copper shrouds now could attracts ^{42}K ions (decay daughter of ^{42}Ar).

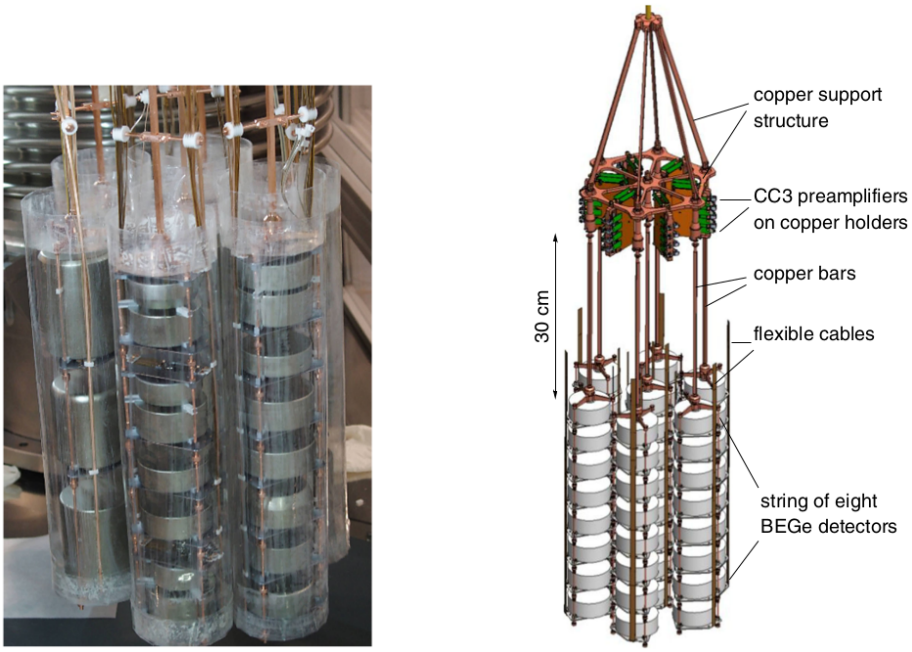

(a) **(b)**

Figure 2.3: Detectors array before being immersed in LAr (a); each string is enclosed in a nylon mini-shroud in order to reduce the deposit of ^{42}K ions on detectors' surface. Scheme of the array and its components (b).

(a) **(b)**

Figure 2.4: Top of the LAr veto system with 9 PMTs and the mounting for calibration sources and bottom part with 7 PMTs (a); fiber curtain that will surround the detectors array and read out by SiPMs (b).

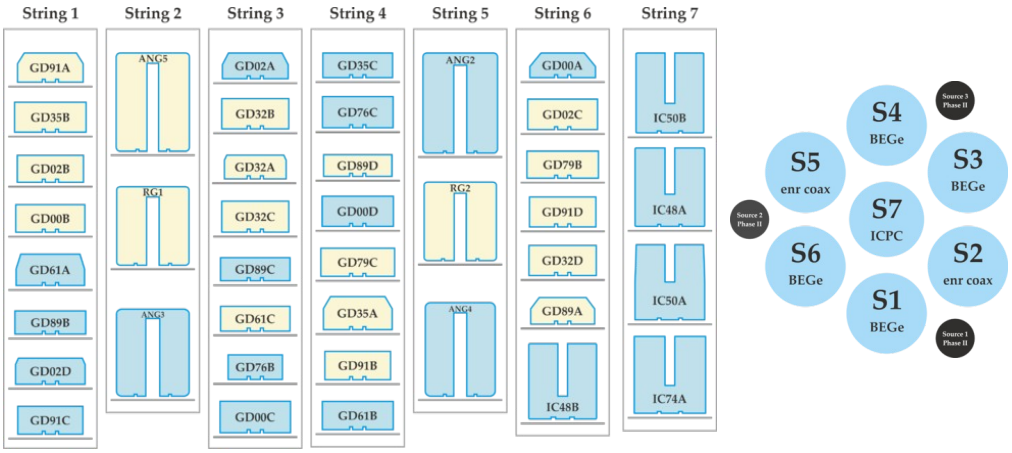

Figure 2.5: Germanium detectors configuration after Phase II$^+$ upgrade; four inverted-coaxial germanium detectors have replaced the three GTF detectors.

2.1.3 Water Tank and Muon veto system

The Gran Sasso overburden of 3500 m w.e. reduces the flux of cosmic muons to about $1.2/(\text{h}\cdot\text{m}^2)$ (many order of magnitude smaller than that at sea level). These muons lose energy by electromagnetic interaction or via inelastic scattering off nuclei, releasing high energy neutrons, that can lead to the production of more isotopes or neutrons. Therefore a 590 m^3 tank filled with ultra-pure water surrounds the LAr cryostat, acting as a shield against radiation and neutrons coming from the external hall and as scintillation medium to detect the Cherenkov light emitted by the passage of cosmic muons by means of 66 8" photomultiplier tubes (PMT). In order to optimize the light collection efficiency a reflective foil has been glued on the inner walls of the water tank and outer walls of the cryostat. Along with the plastic scintillators mounted on the roof of the clean room, the muons rejection efficiency is $> 99\%$ [33].

2.2 GERDA Phase II$^+$ Upgrade

During Phase II another upgrade has been performed as a test bench for the next-generation experiment successor of GERDA in searching neutrinoless double beta decay in ^{76}Ge, the LEGEND experiment. The collaboration aims at building a tonne scale experiment using enriched ^{76}Ge diodes and thus reaching a sensitivity on the half-life of the order of 10^{28} yr. The upgrade involves new germanium detectors, HV and read out cables, the LAr veto system

The natural germanium detectors GTF have been replaced with four inverted-coaxial detectors and were placed in the central string, for a total of 41 detectors (see Figure 2.5). This type of detector still have a bore-hole like semi-coaxial ones (allowing large masses detectors) but the p^+ electrode is dot-shaped and enables pulse-shape discrimination as good as the ones obtained with BEGe detectors.
As for cables, only 3 mils Pyralux® type have been exploited for both power supply and read out because of their radio purity.
The LAr veto system has also been improved by replacing the fiber shroud with another one with 50% more fibers; also a new fiber curtain was fabricated to wrap around the

central string and enhance the detection probability in volumes close to the detectors. All the previous nylon mini-shrouds have been replaced with newer one of the same material.

Chapter 3

Statistical Analysis Concepts

In order to obtain a global model that can reproduce the energy distribution of the GERDA events, simulated spectra of different sources in different locations have been fitted to Phase II^+ data using Bayesian statistics. Before going into deep in the analysis, in this chapter some basic concepts of Bayesian statistics and the algorithm to perform fit on data are presented.

3.1 Bayesian Statistics

At the base of Bayesian statistics there is the idea that probability quantifies the "degree of belief" about an event and it can be framed into a mathematical structure which allows to assign it a numerical value, whether it is more or less likely to happen. This probability should also be computed by taking into account other events logically connected; this means that in this framework probabilities of an hypothesis/event can be continually updated on the basis of new observations/events.
The goal of data analysis is to compare model to experimental data and draw conclusions about the validity of a model as a representation of the data; the model M can be a simple representation of the data (in order to summarize them or make new predictions) or a Physical model. The probability of a model M is denoted with $P(M)$ and satisfies

$$0 \leqslant P(M) \leqslant 1 \tag{3.1}$$

while the probability densities of the parameters $\vec{\lambda}$ are usually continuous functions and must satisfy

$$P(\vec{\lambda}|M) \geqslant 0 \qquad , \qquad \int P(\vec{\lambda}|M)d\vec{\lambda} = 1. \tag{3.2}$$

The quantities $P(M)$ and $P(\vec{\lambda}|M)$ are probability distributions but they have to be interpreted as degree of belief on the model and its parameters instead of frequency distributions [34]. Once we have a model M depending on parameters $\vec{\lambda}$ we can predict the probability of having a particular realization $\vec{y}$ of the physical quantities we want to measure through the function $g(\vec{y}|\vec{\lambda}, M)$ satisfying the following conditions:

$$g(\vec{y}|\vec{\lambda}, M) \geqslant 0 \qquad , \qquad \int g(\vec{y}|\vec{\lambda}, M)d\vec{y} = 1. \tag{3.3}$$

The predictions from the model cannot usually be directly compared to experimental results. An additional step is needed, either to modify the predictions to allow for the

experimental effects, or to undo the experimental effects from the data. Thus it is necessary to add further parameters $\vec{\nu}$ in order to take into accounts these effects and the probability for a given realization $\vec{x}$ of the experimental measurement is given by a different function $f(\vec{x}|\vec{\lambda}, \vec{\nu}, M)$. The parameters of the modeling $\vec{\lambda}$ and that of the experimental effects $\vec{\nu}$ are independent and the latter ones also must satisfy the same conditions as the ones in 3.2 and 3.3.
The procedure for learning from experiment is:

$$P_{i+1}(\vec{\lambda}, \vec{\nu}, M|\vec{D}) \propto f(\vec{x} = \vec{D}|\vec{\lambda}, \vec{\nu}, M) P_i(\vec{\lambda}, \vec{\nu}, M). \tag{3.4}$$

The term P_i is the state of knowledge before performing the experiment and gathering data and indeed depends only on the model parameters (and eventually on experimental effects needed to compare model and experiments). This term (that will be noted as P_0 in the following) is called *prior* probability, it encapsulates all the information we have regardless of the data and different observers may have different prior knowledge about a given phenomenon. The term P_{i+1} is called *posterior* probability and represents our updated state of knowledge after the experiment has been performed. If the function f depends only on parameters $\vec{\lambda}$ and $\vec{\nu}$ and if we compute it for a fixed set of data $\vec{x}$ then it becomes the *likelihood*, a function describing the experimental data. Basically, the learning rule consists in updating our prior knowledge about an event according to the data taken from the experiment, in order to obtain the posterior probability, a probability density function of the parameters of the model of interest. If new data are then available, the posterior can be used as prior probability and it can gets updated using those new data.
In order to have probabilities from previous function we need to normalize 3.4. This can be done by integrating over all possible values of the parameters $\vec{\lambda}$ and $\vec{\nu}$ (assuming that the model we are studying is fixed as well as the dataset $\vec{x}$, like in practical cases) and 3.4 becomes

$$P(\vec{\lambda}, \vec{\nu}|\vec{D}, M) = \frac{P(\vec{x} = \vec{D}|\vec{\lambda}, \vec{\nu}, M) P_0(\vec{\lambda}, \vec{\nu}|M)}{P(\vec{D}|M)} \tag{3.5}$$

where the normalization factor (called also *evidence*) is

$$P(\vec{D}|M) = \int P(\vec{x} = \vec{D}|\vec{\lambda}, \vec{\nu}, M) P_0(\vec{\lambda}, \vec{\nu}, M)\, d\vec{\lambda}\, d\vec{\nu}. \tag{3.6}$$

Written in this form, equation 3.5 is the result of the Bayes theorem. The scheme for updating knowledge is straightforward (although computationally challenging in some cases) and all the information we may require is stored in the posterior probability density function. For example one task we could perform is estimate some of the parameters. In order to do so we do not require all the posterior but only the one of our parameters of interest and this is achieved through *marginalization*. Denoting with λ_i the parameter we want to know the posterior:

$$P(\lambda_i|\vec{D}, M) = \int P(\vec{\lambda}, \vec{\nu}|\vec{D}, M)\, d\vec{\lambda}_{j \neq i}\, d\vec{\nu}. \tag{3.7}$$

At this point the value maximizing the marginalized posterior (mode) is taken as best estimates for the parameter λ_i

$$argmax \left[P(\lambda_i|\vec{D}, M) \right]. \tag{3.8}$$

Note that the value of a given λ_i maximizing the marginalized posterior is not the same as the one maximizing the full posterior pdf; also, if a uniform distribution is chosen as

a parameter's prior then the previous prescription gives the same result as the maximum likelihood method. It is possible to compute credibility intervals such that for example a fraction α of the total area is contained in a certain interval $[\lambda_{lower}, \lambda_{upper}]$.
Sometimes we could have more than one model that could describe our data; this means that we need some tools to perform models comparison and test which hypothesis is in a better agreement with the data. If we do not have a complete set of models, we can use the evidence $P(\vec{D}|M)$ of two different models and compute the *Bayes Factor* BF defined as (assuming two distinct model M_1 and M_2)

$$BF = \frac{P(\vec{D}|M_2)}{P(\vec{D}|M_1)}. \tag{3.9}$$

By looking at 3.6, the evidence is computed by integrating over all possible parameters' values and therefore it encapsulates the information about the validity of the model (the greater the numerical results of the integral the better the overlapping and agreement between prior knowledge and likelihood). This means that, according to equation 3.9, if $BF > 1$ than we have evidence for chosing M_2 over M_1 and the greater this ratio the stronger the evidence; vice versa, if $BF < 1$ then model M_1 should be preferred to M_2 and the smaller the ratio the stronger the evidence.

3.2 Markov Chain Monte Carlo: Theory and Implementation

The computation of the quantities described in the previous section (such as marginalization, normalization, expectation values) becomes hard with standard Monte Carlo methods when dealing with high dimensional parameter space, because these methods could waste time in phase space regions where the function of interest is very small. A Markov Chain Monte Carlo is indeed a method that allows to efficiently sample distributions in high parameters space by dropping the request of sample random numbers independently and instead by performing a random-walk in parameter space. The random walk is achieved through a Markov Chain.
Markov Chains are sequences of random numbers (or vectors of numbers) X_t that have a well defined limiting distribution $\pi(x)$. The fundamental property of these chains is that the probability distribution of the next element in the chain X_{t+1} depends only on the current state (namely X_t) and not on any previous history. A Markov Chain is completely defined by the one step probability transition matrix $P(X_{t+1} = y|P(X_t = x))$. It can be proven under certain assumptions (recurrence, irreducibility, aperiodicity) that the chain is ergodic, i.e. the limiting distribution does not depend on the starting point. A Markov Chain Monte Carlo is a method producing an ergodic Markov Chain whose limiting distribution is the one we are interested in, i.e. $\pi = P(\vec{\lambda}, \vec{\nu}|\vec{D}, M)$.
One of the algorithms to realize a Markov Chain Monte Carlo is the Metropolis algorithm [35] and it works as follow:

1. given that the system is in state $X_t = \vec{x}$, a new proposed state, $\vec{y}$, is generated according to a symmetric proposal function, $g(\vec{y}, \vec{x})$. In our application, a state is a particular configuration of parameter values;

2. the quantity

$$r = \frac{\pi(\vec{y})}{\pi(\vec{x})} \tag{3.10}$$

is then calculated and compared to a random number U uniformly distributed in $[0, 1]$; if $U < r$, then we set $X_{t+1} = \vec{y}$ else we take $X_{t+1} = \vec{x}$.

It is possible to show that, given a reasonable proposal function g, this algorithm satisfies the conditions of a Markov Chain Monte Carlo, and that the limiting distribution is $\pi(\vec{x})$. This then allows for the production of states distributed according to the desired distribution. In particular, this allows for the generation of randomly distributed system states according to complicated probability density functions which have no analytic form. All that is required is that $\pi(\vec{x})$ can somehow be calculated.
The BAT software framework [36] is used in this work in order to implement the Bayesian inference as described above. BAT is a C++ based code, it comes in form of a library and can be interfaced to software packages such as ROOT [37], MINUIT [38] and the CUBA library (containing algorithms for numerical integration) [39].

Chapter 4

GERDA Data Modeling

4.1 Data and Monte Carlo Simulations

The binary raw data format is different according to the various acquisition systems (germanium detectors, muon veto, etc.) and therefore they are all converted to a common standardized format in order to provide a unique interface. MGDO (MAJORANA-GERDA Data Objects) [40] is a software library jointly developed by GERDA and MAJORANA collaborations containing general purpose interfaces and analysis tools. Custom data objects available in MGDO are used to store events, waveforms and other DAQ data (time stamps, flags) and are stored as ROOT files. The set of these files is named TIER1; the information stored here and in raw data is expected to be equal and thus data blinding is performed at this level. Events with an energy in the window $Q_{\beta\beta} \pm 25\,keV$ are not exported to TIER1 but remain saved into raw data backup.
The software framework GELATIO [41] contains nearly independent and customizable modules that are applied to the input TIER1 waveforms. The results (pulse, amplitude, rise time, average baseline, etc.) are stored as new ROOT files called TIER2. A detailed description of the analysis modules is presented in [42]. Also higher level TIERi containing additional parameters evaluated for more advanced analysis (e.g. calibrated energy spectra) can be created.
The analysis described in this work has been carried out on calibrated data (taken during PhaseII$^+$) before applying high level cuts (such as LAr veto and pulse shape discrimination), even though all events need to pass a number of quality cuts in order to discard unphysical ones.
By defining multiplicity of an event as the number of germanium detectors in which the energy deposition exceeds a given threshold, we can divide the dataset into *M1* (multiplicity one) and *M2* (multiplicity two). *M1* events are further split into three datasets according to the different geometries of the detectors called *M1-enrBEGe*, *M1-semiCoax* and *M1-invCoax*. The energy in *M2-enrAll* events is the sum of the two germanium detectors triggered. The acquired spectra are showed in Figure 4.1 and 4.2. For the single-detector data, the following features are most noticeable: the β-decay of ^{39}Ar dominates the spectrum up to 565 keV while between 600 and 1500 keV the most prominent component is the continuous spectrum of $2\nu\beta\beta$ decay of ^{76}Ge. Two γ lines at 1461 and 1525 keV can be attributed to ^{40}K and ^{42}K; further visible γ lines belonging to ^{208}Tl, ^{214}Bi and ^{228}Ac are indicated in the figure. The highest energies displayed are dominated by a peak-like structure emerging at 5.3 MeV with a pronounced low energy tail. This is a typical spectral feature of α particles and can, here, be attributed to ^{210}Po decay on the thin detector p$^+$

surfaces [43]. All these components contribute also to *M2-enrAll* except for ^{39}Ar, $2\nu\beta\beta$ and high energy α-components. This is due to the short range of α (tens of μm) and β particles (typically smaller than 1.5 cm) in LAr and germanium with respect to the distance between detectors which is of the order of several cm.

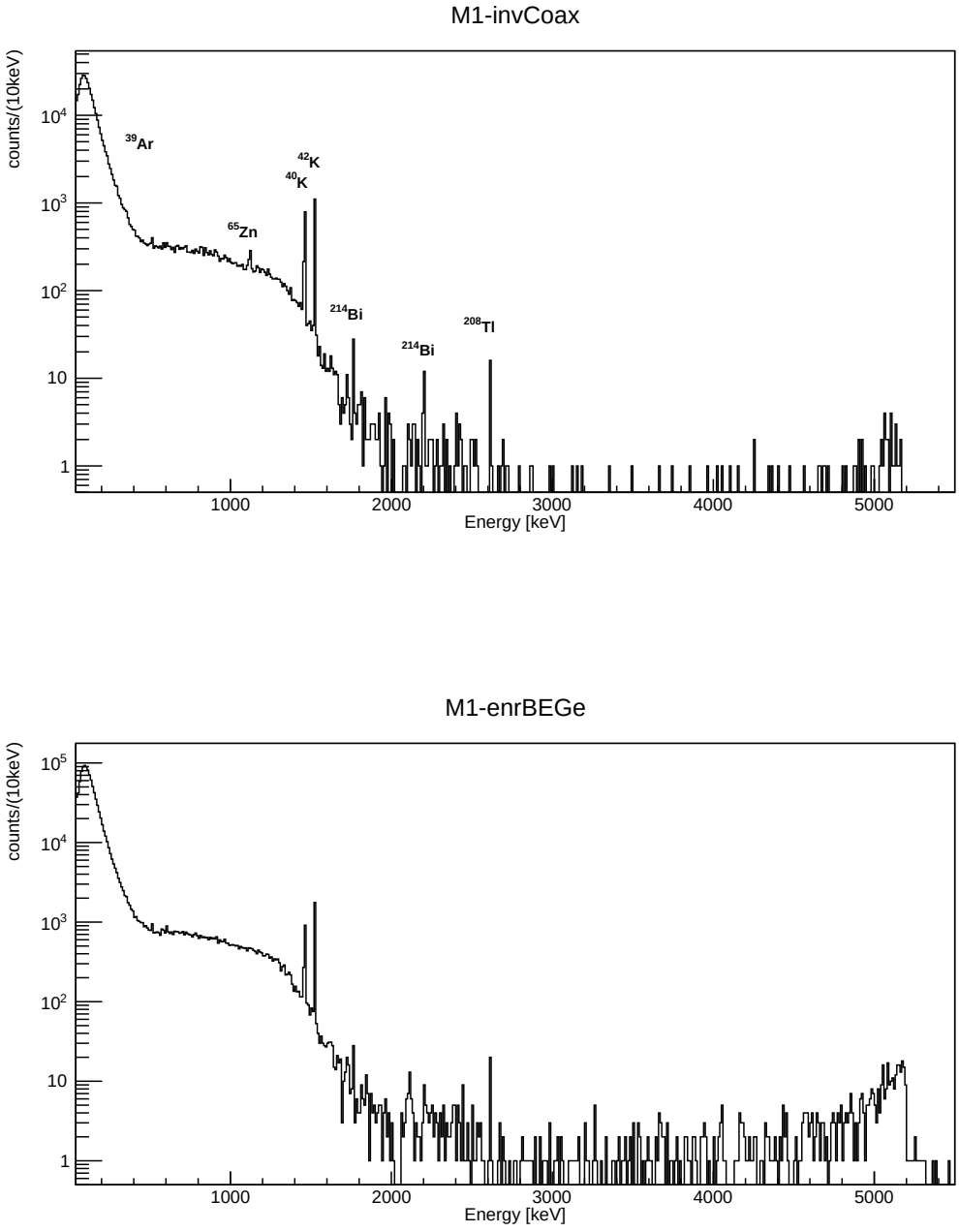

Figure 4.1: PhaseII$^+$ data divided into detector type (invCoax, enrBEGe and semiCoax) and coincidence events. Here the inverted Coaxial and BEGe detectors spectra are shown as well as some of the most prominent γ lines. ^{65}Zn is visible only in *M1-invCoax* dataset.

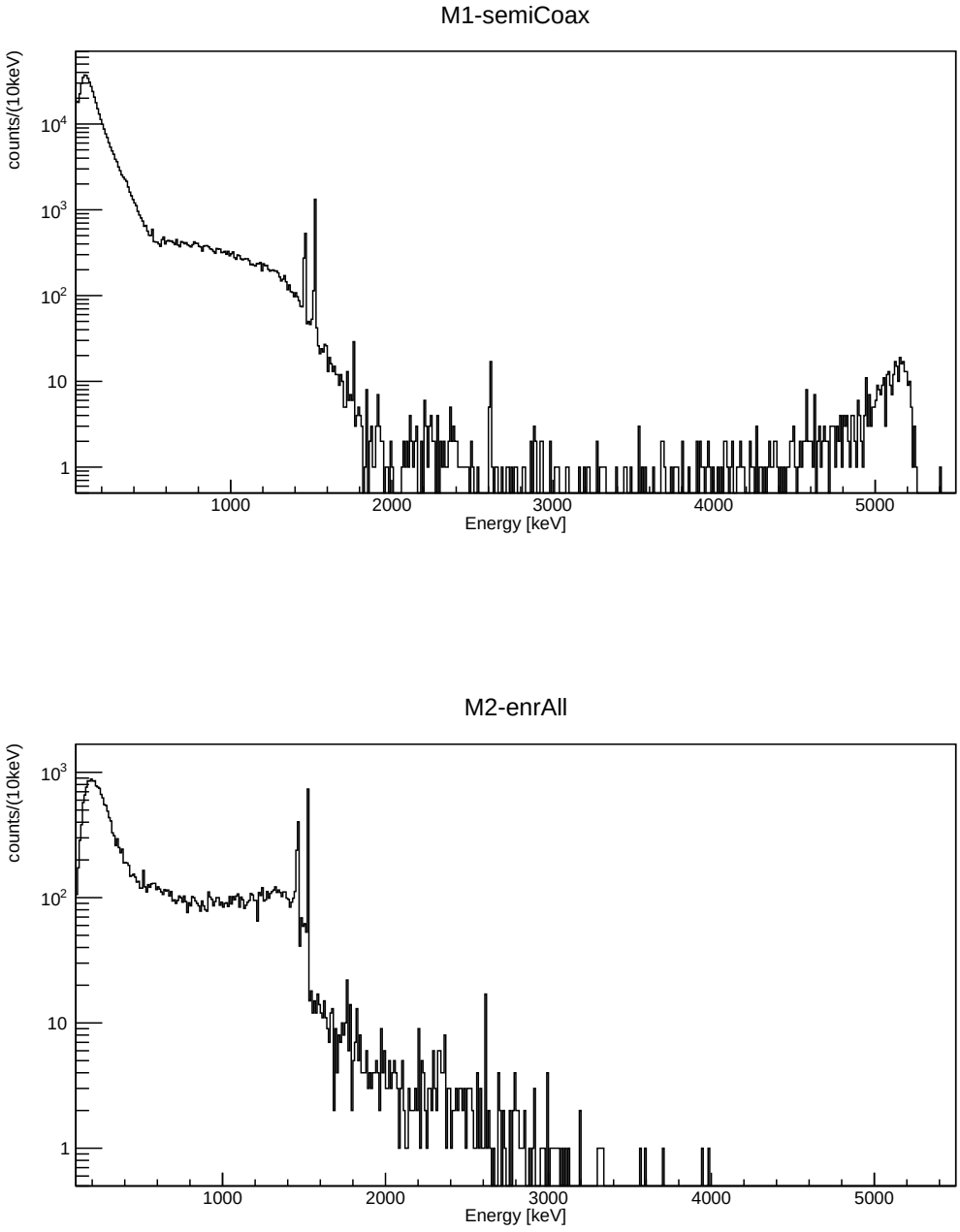

Figure 4.2: PhaseII$^+$ data divided into detector type (invCoax, enrBEGe and semiCoax) and coincidence events. Here semiCoaxial detectors and coincidence events spectra are shown.

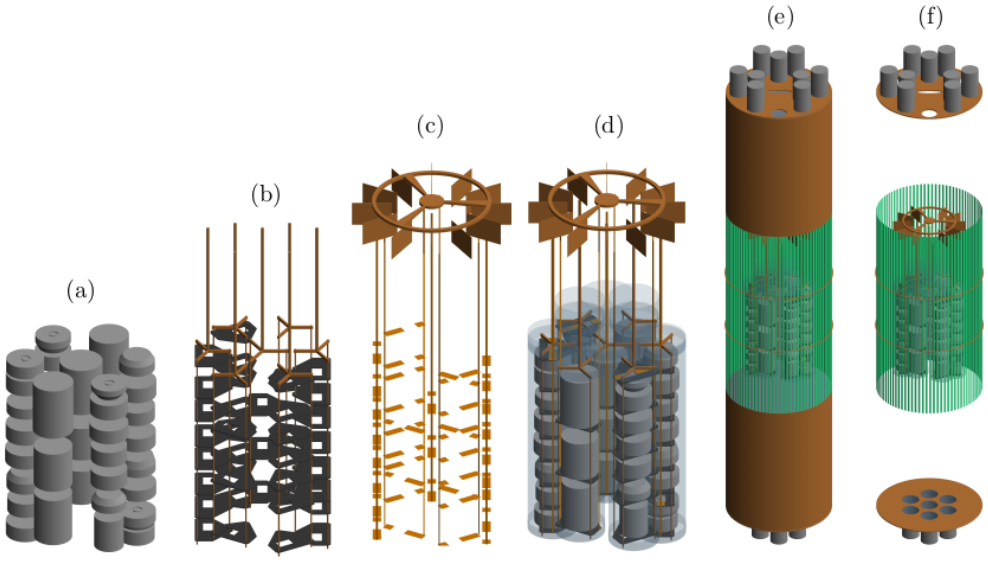

Figure 4.3: Implementation of the GERDA array in MAGE. From left to right: a) GERDA detectors; b)detectors low mass holders, composed of silicon plates and copper bars; c) HV and signal flexible flat cables with front-end electronics on top; d) the full array with also the nylon minishrouds; e)the full LAr veto system, including wavelength shifter fibers, PMTs and the Tetratex®-coated copper shrouds; e) the full insturmentation with LAr veto system without copper shrouds. Picture taken from [44].

The Probability Density Functions (PDFs) used to model contributions to the energy spectra are obtained from Monte Carlo simulations generated through the MAGE simulation framework [45], based on GEANT4 v.10.4 [46][47][48]. MAGE contains a software implementation of the GERDA PhaseII$^+$ detectors as well as the assembly and the other surrounding hardware components. A picture of the MAGE implementation can be found in Figure 4.3. Intrinsic $2\nu\beta\beta$ of ^{76}Ge inside the detectors and the background events coming from contamination sources are simulated in and around the assembly, namely: on the p^+ and n^+ contact of the detectors, homogeneously distributed in LAr, in the detector holders and their components, in the nylon mini-shroud surrounding the detectors, in the fiber-shroud and in in the high-voltage cables and the signal cables.
The energy spectrum of the two electron emitted in the $2\nu\beta\beta$ was sampled according to distributions described in [49] implemented in DECAY0 [50]. All the other background sources simulated in different parts of the apparatus are described in the next section. Along with detectors data and MC simulations, the structural components of the setup have been screened for their radio-purity before deployment. Screening measurements were performed using γ-ray spectroscopy HPGe or mass spectrometry with Inductively Coupled Plasma Mass Spectrometers (ICP-MS) during PhaseII. Materials close to the detectors have been screened for radioactive contaminations originating from the ^{238}U and ^{232}Th decay chains, ^{40}K and ^{60}Co. The activities and upper limits used in this work are listed in Table 4.1. These measurements will be used in the following sections as prior distribution of the activity of the background sources in different part of the apparatus.

Part	Material	Method	^{228}Ra (μBq)	^{226}Ra (μBq)	^{228}Th (μBq)	^{60}Co (μBq)	^{40}K (mBq)	^{238}U (mBq)
cables	Tecnomec 3 mil	γ spec.	< 153	< 103	< 126	< 21	3.01 ± 0.82	< 18.0
LAr veto	outer BCF-91A fibers	ICP-MS	177 ± 53	93 ± 28	177 ± 53	-	3.1 ± 0.9	0.93 ± 0.028
	inner BCF-91A fibers	ICP-MS	24 ± 7	12 ± 4	24 ± 7	-	0.41 ± 0.01	0.012 ± 0.004
minishroud	coated+glued	ICP-MS	19 ± 5	46 ± 14	19 ± 5	-	> 1.8	0.046 ± 0.014

Table 4.1: Activity of setup components deployed during PhaseII$^+$ upgrade calculated from radio-purity screening measurements. Values in gray can be used as priors for background modeling as they are; values in gree are (partly) derived from ICP-MS measurements under the assumptions of secular equilibrium in the U/Th decay chains; values in light blue have to be multiplied by 2/3. The latter is an approximation for the shortening of the cables before deployment in GERDA.

4.2 Expected Background Sources

As already mentioned in the previous section, some of the main sources of background are isotopes belonging to ^{232}Th and ^{238}U decay chains. Simulated isotopes are ^{214}Pb and ^{214}Bi from ^{238}U and ^{228}Ac, ^{212}Bi and ^{208}Tl from ^{232}Th; daughter nuclei are supposed to be in secular equilibrium with their respective parent nucleus. All of them undergo β-decay and therefore their decay products consist in γ or β particles having an energy greater than 520 keV. The most intense γ-ray that can effect the background around $Q_{\beta\beta}$ due to Compton scattering is the one at 2614 keV of ^{208}Tl. These contaminants are expected to be present in the major part of the components. Less energetic particles from the remaining constituents in the chain do not enter the energy window which is considered in the presented analysis.
A significant fraction of the components deployed in GERDA is made of copper that can be produced with high radio-purity but it is potentially activated by cosmic rays producing the long-lived isotope ^{60}Co.
^{40}K is found in nearly all screened materials and is one of the main sources of environmental radioactivity along with U/Th chains. Construction materials were not optimized for ultra-low ^{40}K content because its Q-value is well below $Q_{\beta\beta}$.
^{42}K is produced after the decay of the cosmogenically produced ^{42}Ar in LAr. The distribution of ^{42}K in LAr is quite likely to be inhomogeneous due to the drift of ionized decay product induced by the electric field generated by high-voltage cables and detectors and convection. ^{42}K β-decay to ^{42}Ca with a Q-value of about 3525 keV, well above $Q_{\beta\beta}$. In order to detect the emitted β particle it is necessary for the decay to happen within a distance of a few centimeters from the surface of the detectors. Therefore two distinct simulations are used in order to disentangle potassium components inside and outside the nylon minishrouds.
α particles are also another source of background due to mainly ^{210}Po; the n^+ lithium-diffused electrode acts as a barrier while boron-implanted p^+ electrode is thin enough ($\sim 0.5\,\mu$m) to let αs release part of their energy in the active volume, leading to a peak at about 5 MeV with a long tail.
In addition to the previous sources, an event excess is observed at 1124 keV in *M1-invCoax* which is attributed to the decay of ^{65}Zn in the germanium. ^{65}Zn is produced in the reaction $^{76}Ge(\mathrm{n},\alpha 2\mathrm{n})^{65}Zn$ induced by cosmic rays. InvCoax detectors have been deployed in GERDA shortly after being produced, so the 1124 keV line (γ de-excitation of ^{65}Cu coincident with K-shell X-rays) can be seen.

4.3 Background Model

The multivariate statistical analysis, which is used to model and disentangle the background in its components, runs on the four binned datasets: *M1-enrBEGe*, *M1-semiCoax*, *M1-invCoax* and *M2-enrAll*. Moreover, the count rate per detector is used for the two potassium γ lines.
Assuming that the number of events in each bin follows a Poisson distribution the likelihood function for a binned dataset reads $\prod_i^{N_{bins}} Pois(n_i;\nu_i)$, where n_i is the experimental number of counts in i-th bin and ν_i the expected one. In particular, $\nu_i = \sum_{k=1}^{m} \nu_i^{(k)}$ is calculated as the sum (for a given bin) of the contributions from each background component k; $\nu_i(\lambda_1, ..., \lambda_m)$ is a function of the m parameters of interest λ_j (isotope activities, $2\nu\beta\beta$ half-life, etc.). The complete likelihood function adopted for the present analysis combines the datasets *M1-enrBEGe*, *M1-semiCoax*, *M1-invCoax* and *M2-enrAll*:

$$\mathcal{L}(\lambda_1, ..., \lambda_m | data) = \prod_{d=1}^{N_{dat}} \prod_{i=1}^{N_{bins}} Pois(n_{d,i}; \nu_{d,i}) \tag{4.1}$$

The statistical inference is made within a Bayesian framework. Hence, to obtain posterior probabilities for the free parameters of interest λ_j , the likelihood defined in 4.1 is multiplied according to the Bayes theorem by a factor modeling the prior knowledge of each background component (screening measurements as reported in Table 4.1). Gaussian *pdf*s were chosen for contaminants' activity measurements while an exponential distribution[1] was chosen if only upper limits were available. The computation is performed using a Markov Chain Monte Carlo (MCMC) and is implemented using the BAT software suite. Posterior probability distributions of any observable that is not a free parameter of the likelihood function, like background index estimates, are obtained by sampling the desired parameter from the MCMC. A p-value estimate is provided as a goodness-of-fit measure by adopting the algorithm suggested in reference [51] for Poisson-distributed data. It has to be kept in mind that this p-value estimate, however, is not as well suited for model comparison as is for instance a Bayes factor; e.g. the number of free parameters is not taken into account while a Bayes factor always penalizes models that add extra complexity without being required by the data.

4.3.1 K Model

The two full-energy lines of ^{40}K and ^{42}K at 1461 keV and 1525 keV are distinct features of the energy spectrum shown in Figure 4.1 and 4.2. Being a relevant source of background for double-beta decay, the two potassium isotopes play a crucial role in the background modeling process in GERDA. Uncertainties in their origin and distribution propagate directly to searches for exotic physics like Majorons, Lorentz invariance-violating processes or decay modes to excited states of $2\nu\beta\beta$ decay in which the shape of the $2\nu\beta\beta$ decay spectrum is a unique feature.
Two windows around the potassium γ lines (1461.4 keV for ^{40}K and 1524.4 keV for ^{42}K) have been projected in detector index space such that, for single detector datasets, each point represents the number of counts in detector i within the considered energy window. For the two-detector dataset the detector space is two dimensional and each point represents the total number of counts in detector i and j within the considered energy window. The intervals for the potassium events (denoted with K40 and K42 in the following) are reported in Table 4.2; Figure 4.4 shows the energy regions selected in *M1* data. Also, three side-bands (SB1, SB2 and SB3) have been selected and are used to estimate the continuum below and above the γ-lines (see Table 4.2 and Figure). Considering also the further subdivision into *M1* and *M2* datasets a total of 5×2 energy regions have been fitted. In this regions the major contributions the major contributions beside the potassium events are expected to come from $2\nu\beta\beta$ and ^{214}Bi; contributions from other isotopes are expected to be irrelevant in the energy windows considered here.

As for the likelihood used to fit the data, equation 4.1 can be factorized into uncorrelated parts that can be studied individually and in this case, where 5×2 energy ranges are considered, becomes:

[1] parameters were chosen in such a way that 90% of the distribution area was under the experimentally measure upper limit on the activity

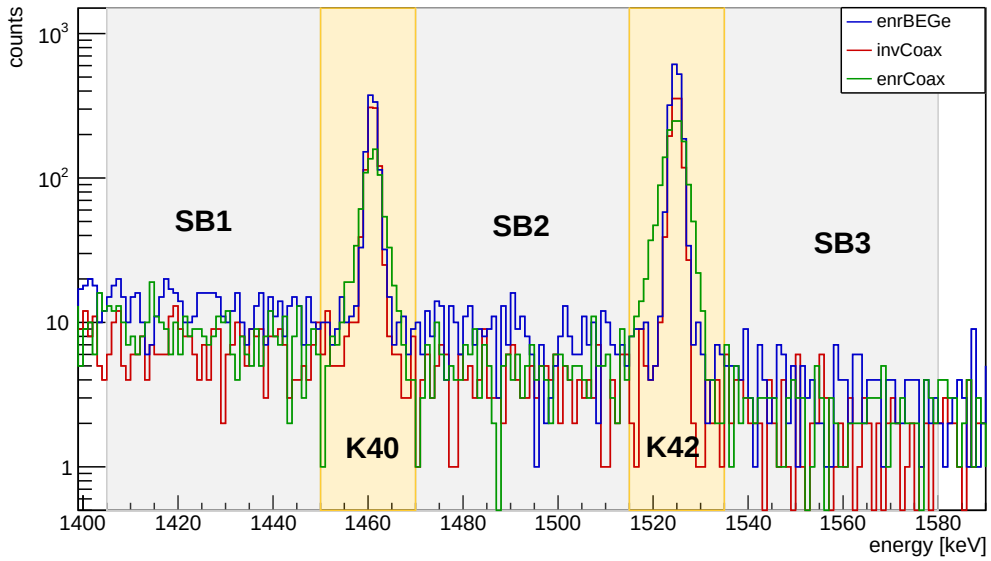

Figure 4.4: Visual representation of the five energy ranges defined for the potassium tracking analysis. Exact interval can be found in Table 4.2

	M1 [keV]	M2 [keV]
K40	[1450, 1470]	[1450, 1470]
K42	[1515, 1535]	[1515, 1535]
SB1	[1405, 1450]	[1405, 1450]
SB2	[1470, 1515]	[1470, 1515]
SB3	[1535, 1580]	[1535, 1580]

Table 4.2: Energy windows for the potassium tracking analysis. K40 and K42 ranges have been enlarged with respect to PhaseII analysis due to the worsening of semi-coaxial detectors resolution.

$$\mathcal{L}_K(\lambda_1, ..., \lambda_{m'}|n) = \prod_{d=1}^{N_{dat}} \left\{ \prod_{i=1}^{N_{det}} Pois(n_{d,i}^{\mathrm{M1}}; \nu_{d,i}^{\mathrm{M1}}) \times \prod_{j<k}^{N_{det}} Pois(n_{d,i}^{\mathrm{M2}}; \nu_{d,i}^{\mathrm{M2}}) \right\} \tag{4.2}$$

As for the prior distributions, Gaussian probability density functions have been used for ^{40}K activity where screening measurements were available; on the contrary, ^{42}K is dissolved into LAr and therefore no screening measurements are available. This means that the prior considered is a uniform distribution. The analysis flow starts with a construction of a first, preliminary model; this resulting model, however, gives a non-satisfactory description of data and the posterior distributions for the ^{40}K components are significantly shifted to higher values with respect to the prior distributions, indicating a surplus. To find a better agreement with physics data while keeping the model as simple as possible, additional components using uniform priors are included one at a time in the fitting procedure, and the Bayes factor (as described in the previous chapter) is calculated between the extended and the preliminary model. The model is iteratively updated by adding the component that results in the highest Bayes factor until no Bayes factor is larger than 10.

Iter-1		Iter-2		Iter-3	
K40Holders	10^{120}	K40Holders	10^{-2}	K40Holders	10^{-2}
K40InFiber	10^{27}	K40InFiber	10	K40InFiber	~ 1
K40Ms	10^{190}	K40OutFiber	~ 1	K40OutFiber	~ 1
K40OutFiber	10^{8}	K42Above	10^{108}	K42n+invCoax	10^{15}
K42Above	10^{100}	K42n+invCoax	10^{18}		
K42n+invCoax	10^{18}				

Iter-4		Iter-5	
K40Holders	10^{-1}	K40Holders	10^{-2}
K40InFiber	10^{2}	K40OutFiber	10^{-1}
K40OutFiber	~ 1		

Table 4.3: Bayes factor computed at each iteration of the analysis procedure between the new model with the new parameter and the model accepted at previous step; in blue is the parameter added in a given iteration (if any). After the first parameter has been added to the base model, the Bayes factor drops rapidly by many order of magnitude because, when comparing similar models, it always penalizes complexity (i.e. number of parameters).

4.4 Results

In both potassium tracking and full-range fit, possible sources of background having a mean number of events compatible with zero have been removed. In the potassium tracking analysis, prior distributions for the expected number of events have been included only for ^{40}K.
The isotopes in the minimal model chosen for potassium analysis are:

- $2\nu\beta\beta$ for semiCoax, invCoax and BEGe (leading contribution after potassium);
- ^{40}K in cables (K40Cables);
- ^{42}K in a cylindrical volume centered on the detector array($h = 250$ cm, $r = 100$ cm) and then divided into outside the nylon minishrouds (K42LArSurr, used in the base model) and inside them;
- ^{214}Bi in cables (Bi214Cables).

^{40}K (but also ^{214}Bi) was placed in cables because they proved to be one of the most contaminated part of the apparatus during previous data taking and background study; ^{214}Bi was chosen just as "dummy" variable in order to account for those events not belonging to potassium or double beta decay. The number of these events in the energy region considered is very low and makes impossible discriminating between different location in the apparatus. Simulations to be added are:

- ^{40}K in nylon minishroud (K40Ms), detector holders (K40Holders) and scintillating fibers both within the array (K42InFibers) and surrounding (K42OutFibers);
- ^{42}K (homogeneously distributed simulated inside LAr) has been studied inside detectors minishroud (K42InMs), above the array where signal cables could have attracted it (K42Above) and over the n^+ electrode of detectors.

K42InMs and semiCoax and BEGe ^{42}K numbers of events were compatible with zero

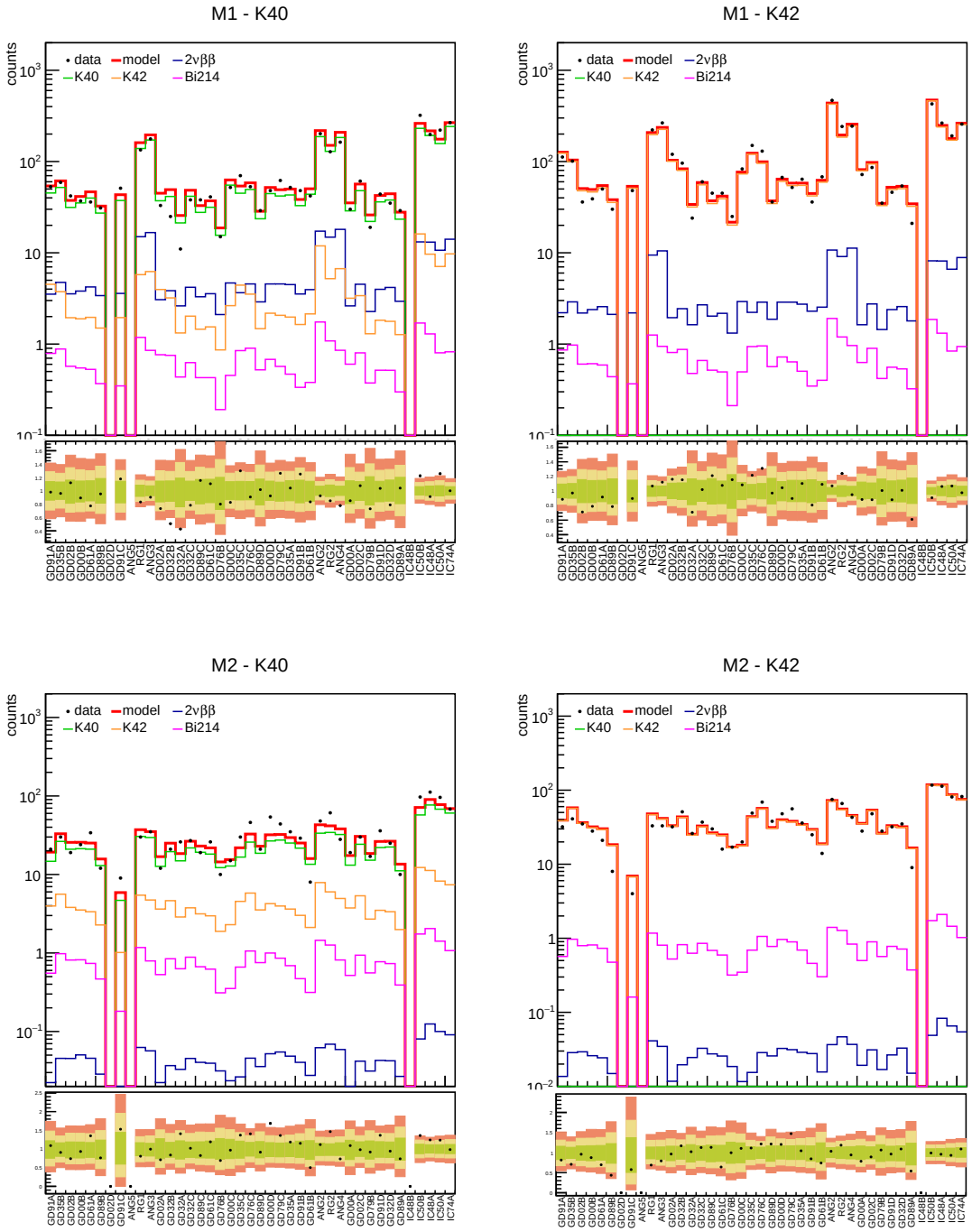

Figure 4.5: Decomposition of the energy windows corresponding to the two potassium lines for each detector (detector space): single-detector (top) and two-detector (bottom) data. Different components of the same isotopes in the potassium model are merged together for visualization purposes. The number of ^{40}K events under the 1525 keV energy peak of ^{42}K is zero because the former decays by electron capture (and this means that no electrons/positrons are emitted to be detected; also the Q-value does not allow the emission of more energetic γ rays than 1461 keV) or by β^- and again its Q-value is below ^{42}K peak.

throughout the analysis and have not been considered. After five iterations no more parameters could result in a model with a Bayes factor greater then 10 and so the iterations

stopped. Details about iteration and parameters added to final potassium model are presented in Table 4.3. Fit result and residuals are shown in Figure 4.5. The only two parameters left out of the model are K40Holders and K40OuterFiber: these new added material, being so close to the detector array induce a non-negligible background while the surrounding fibers does not contribute. As for K40Holders, a well known problem is the degeneracy of some *pdf*s, i.e. simulations of the same isotope but in different locations may have the same profile. Therefore the two activities will be correlated and it is not possible anymore to discriminate which is the source of radiation. Thus, for example as in this case, if K40Cables is present then K40Holders does not give any further information about the description of the data and therefore will never be accepted in the model. On the other hand, an initial model with K40Holders would never accept during iterations K40Cables. This is exactly what has been done; the procedure is the same as the one showed before and the final model would have potassium into the holders rather than in cables (actually K40Holders would also replace K40InFIber, making it evident the difficulty of discriminating with accuracy among different sources very close to the array) and the two model are equivalent (BF ~ 1).

The posterior probability distribution for ^{40}K and ^{42}K just found are then incorporated into the full range fit as prior *pdf*s for the the two potassium isotopes of interest. For all other isotopes, screening measurements have been used (if present) as discussed before. Alpha particles contamination have not been considered because of the very low number of events at energies greater than 3 MeV in PhaseII$^+$ data and its small contribution to the background at $Q_{\beta\beta}$.
Datasets have been fitted simultaneously using the same parameters (isotopes activities). Fit range chosen starts at 565 keV, the end point of ^{39}Ar whose low-energy contribution is not relevant for the present analysis, up to 2150 keV, just above last prominent ^{214}Bi γ line. The results are reported in Figure 4.6 and 4.7; a list of the parameters properties extracted from their posterior distributions as well as the background index[2] for *M1* datasets in each component are reported in Table 4.4. The prior distribution exploited in the analysis (flat, gaussian or exponential) is also specified, even though ^{40}K screening measurement were inserted only in potassium model. In order to disentangle ^{42}K β and γ contributions to the background, the volume inside and outside the minishroud is separated. As already seen during potassium analysis, ^{42}K activity inside nylon minishrouds is compatible with zero and it is not inserted into global model. In general, components close to the detectors array generated much more events than distant ones and this happens also in this case by looking at Table 4.4: the volume around the array has a higher BI than the one just above the array (where ^{42}K can be attracted from HV cables). However ^{42}K activity on the n$^+$ electrode is non-negligible only for invCoax detectors and according to these results represents a huge source of background, even greater than total BI for the the other two types of detector.
Given the great energy resolution of GERDA it is possible to discriminate between $2\nu\beta\beta$ and $0\nu\beta\beta$ and in fact the BI due to the former process is zero. Most counts in fit range are due to the $2\nu\beta\beta$ of ^{76}Ge and its continuous distribution dominates the spectrum up to 1.9 MeV. Although a more accurate analysis is required, an estimate of its half-life can be extracted from this analysis for the three detector types and they are all compatible with the one reported in [13], although a systematic discrepancy between the half-life predicted with BEGe detectors and with SemiCoax detectors is found. The half-life predicted with

[2]Background Index (BI) is defined as the number of counts over exposure and energy in the energy window from 1930 keV to 2190 keV excluding the region around $Q_{\beta\beta}$ ($Q_{\beta\beta}\pm5$ keV) and the intervals 2104±5 keV and 2119±5 keV, which correspond to known γ-lines from ^{208}Tl and ^{214}Bi.

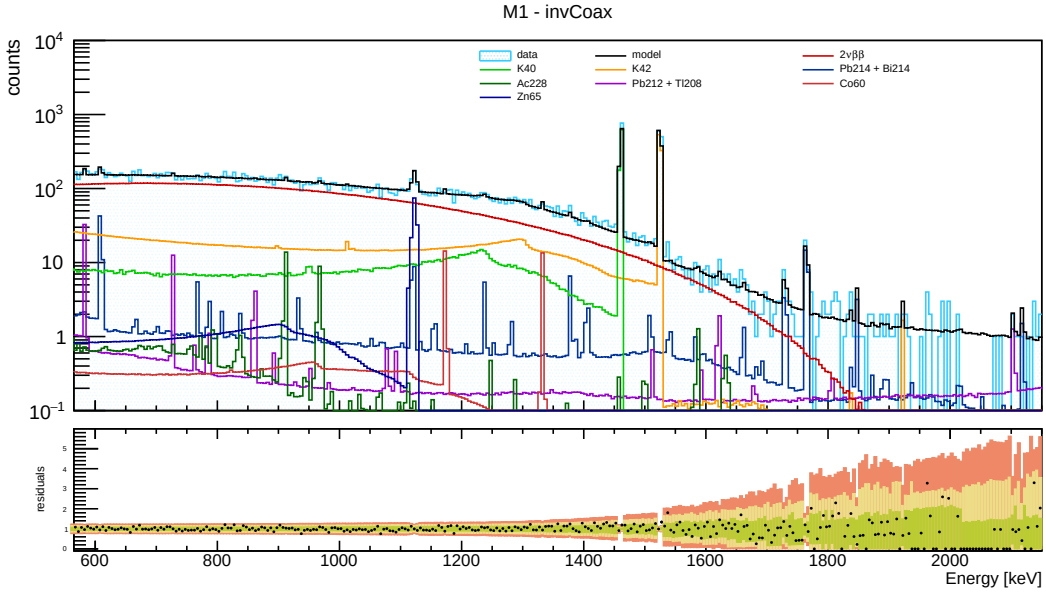

(a)

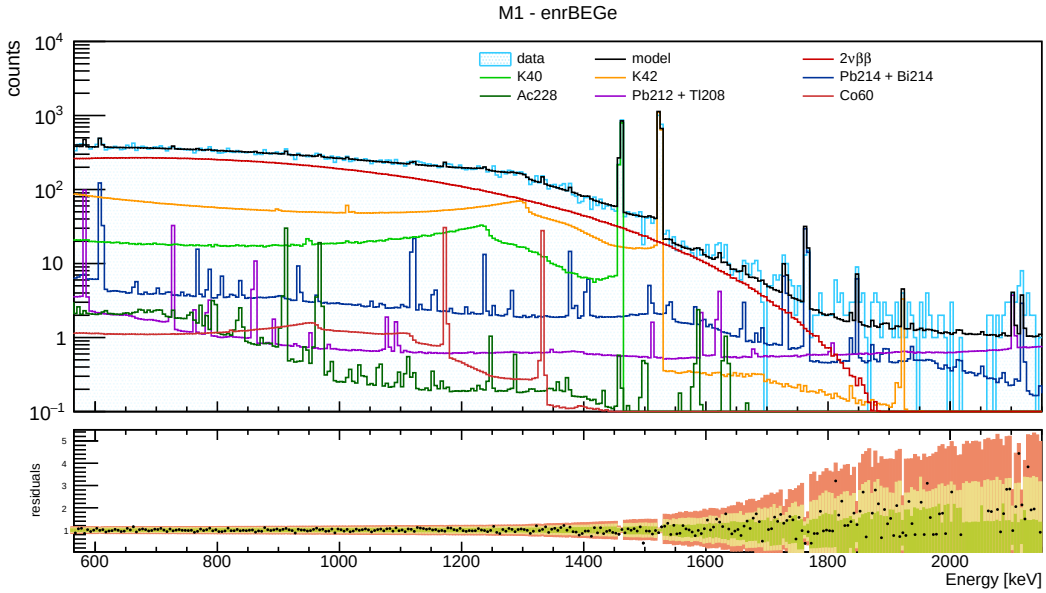

(b)

Figure 4.6: Global model fit results with residuals of *M1-invCoax* and *M1-enrBEGe* datasets. Fit range is [565,2150] keV and the.The presence of a peak structure at around 1100 keV in the first dataset is perfectly described by the decay of ^{65}Zn. There is no presence of this contaminant in other *M1* datasets nor in *M2-enrAll*.

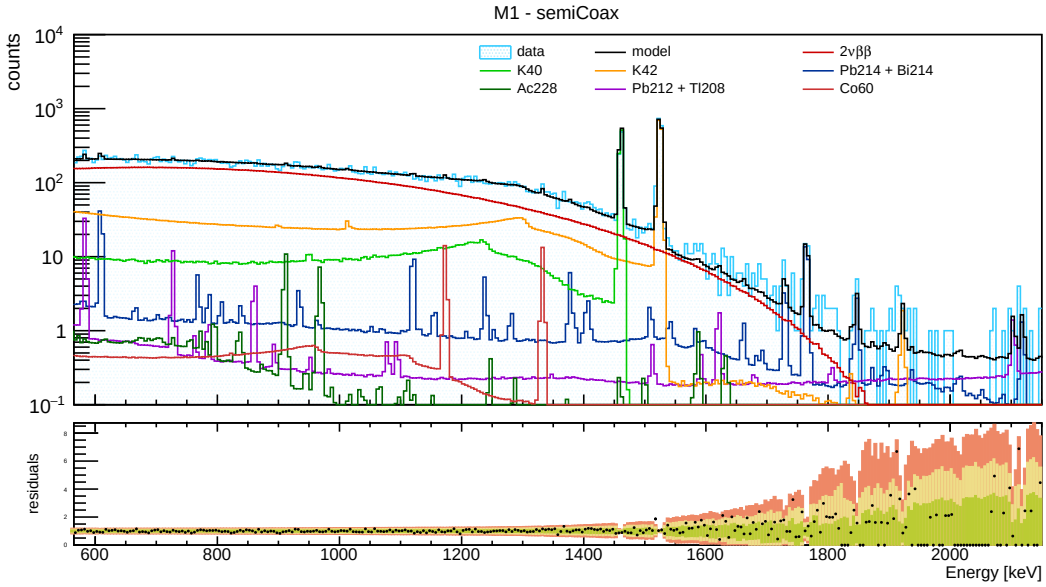

(a)

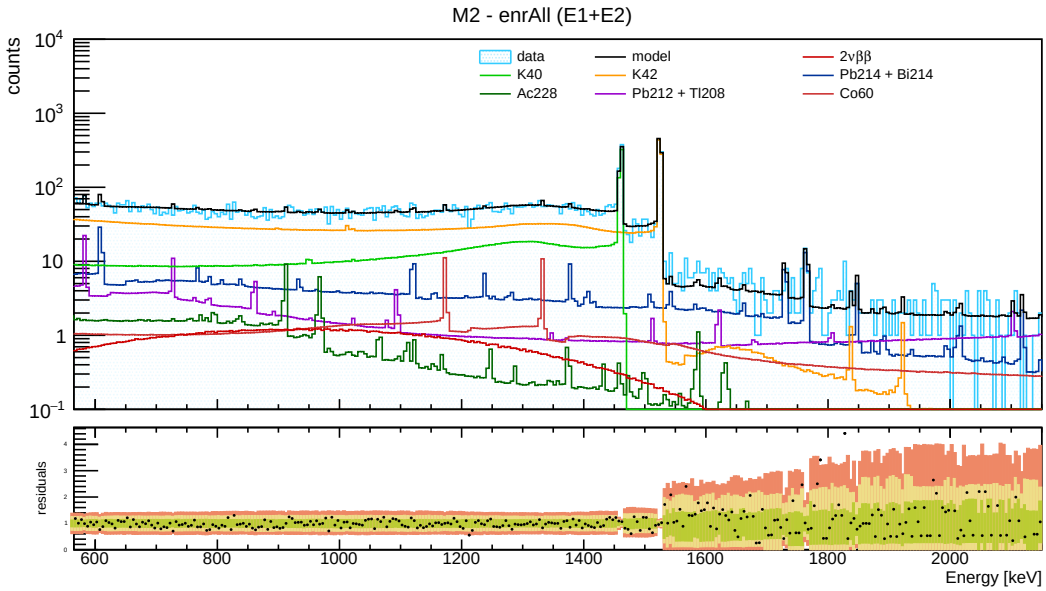

(b)

Figure 4.7: Global model fit results with residuals for *M1-semiCoax* and *M2-enrAll* datasets. *M2-enrAll* events are the sum of the deposited energy in the two triggered detectors and are mainly due to Compton scattered photons. As a matter of fact the $2\nu\beta\beta$ contribution is not present.

InvCoax detectors, on the other hand, seems to give the same results extracted from the SemiCoax detectors. There is a clear evidence for a systematic underestimation of the SemiCoax and InvCoax detector active volume, or overestimation of the BEGe detector active volume, or even a more complex situation.
The most important contributions to the background around $Q_{\beta\beta}$ are given by ^{208}Tl and ^{214}Bi both located in HV and signal cables (for *M1-enrBEGe* and *M1-semiCoax* datasets) that in PhaseII^{+} have been optimized according to screening measurements to enhance materials radio-purity.
Final BI prior to active background cuts (Table 4.4) for *M1-enrBEGe* and *M1-semiCoax* found in this model are lower than the ones reported in [44] for the first part of PhaseII and this demonstrates that, after the upgrade, background events rate has not increased but rather lowered. Inverted Coaxial detectors have been employed for the first time in PhaseII^{+} and therefore no previous BI estimate is available; its value is greater than PhaseII first phase estimates but anyway not far away.

source	[prior] location	units	global mode	marg. mode and 68% CI	screening	BI at $Q_{\beta\beta}$ 10^{-3} cts/(keV·kg·yr)		
						M1-enrBEGe	M1-semiCoax	M1-invCoax
$2\nu\beta\beta$	[f] BEGe detectors	10^{21} yr	2.09	2.09 [2.07,2.10]	-	0	0	0
	[f] invCoax detectors		1.89	1.89 [1.87,1.91]	-			
	[f] semiCoax detectors		1.91	1.91 [1.89,1.92]	-			
^{228}Ac	[e] cables	μBq	179	190 [140,250]	<153	0	0	0
$^{212}Bi + {}^{208}Tl$	[e] cables	μBq	708	692 [624,763]	<103	6.8	4.1	4.3
	[g] nylon minishrouds		21	20 [15,26]	19 ± 5	0.22	0.20	0.21
^{60}Co	[e] detectors holders	μBq	63	65 [51,76]	<100	0.44	0.43	0.47
^{40}K	[g] cables	mBq	2.27	2.52 [1.99,3.05]	3.01 ± 0.82	0	0	0
	[g] LAr inner fibers		0.53	0.53 [0.45,0.64]	0.41 ± 0.12			
	[f] nylon minishrouds		17.8	17.7 [17.2,18.1]	-			
^{42}K	[f] volume above array	mBq	388	383 [370,400]	-	0.25	0.17	0.26
	[f] volume outside minishroud	Bq	1.9	1.9 [1.8,2.0]	-	0.62	0.68	0.50
	[f] n^+ invCoax	mBq	0.27	0.27 [0.24,0.32]	-	0	0	18.9
$^{214}Pb + {}^{214}Bi$	[e] cables	μBq	594	590 [540,640]	<103	3.0	2.1	2.5
	[g] nylon minishrouds		53	52 [39,67]	46 ± 14	0.25	0.28	0.34
^{65}Zn	[f] invCoax detectors	μBq	51	52 [44,66]	-	0	0	0
total						11.6	7.96	27.5

Table 4.4: Parameters obtained from full range fit. Global and marginalized mode along with 68% C.I. are reported as representatives of the posterior parameter distribution. BI at $Q_{\beta\beta}$ prior active background suppression is listed for each component and each analysis data set. The original type of prior distribution is marked with [f] for flat, [g] for Gaussian and [e] for exponential.

Conclusions

In this thesis I studied the background decomposition of the events detected by GERDA experiment whose aim is to observe for the first time ever the neutrinoless double beta decay. The discovery of this process would prove the non conservation of total leptonic number and the Majorana nature of neutrinos and could give an insight about neutrinos' mass generation mechanism and the origin of the matter/amtimatter asymmetry in the Universe.
Being able to detect such a very rare event ($T_{1/2} > 10^{26}$ yr) means minimizing as much as possible background while increasing the active mass that could undergo $0\nu\beta\beta$. After the upgrade in 2018 of the experiment (new detectors added and improved LAr veto) a new assessment of the isotopes contributing to the background was necessary. The first step was potassium tracking analysis, since ^{40}K and ^{42}K are the major sources of events in $2\nu\beta\beta$ region and ^{42}K also contributes to the background near $Q_{\beta\beta}$. I started with a minimal base model and then continued with adding more parameters according to Bayes factors, comparing the base model and the new possible one. The results are then inserted into the full range fit as prior information on ^{40}K and ^{42}K activities. Both models suffer from correlation among parameters: *pdf*s profile is equal to the same isotope in different locations leading to the impossibility of reconstructing the exact position of the background source. As a matter of fact, in potassium tracking, two models that differs only for ^{40}K in cables or detectors holders give exactly the same results. This indetermination propagates also in the full range model.
The final full range model consists of 16 parameters, chosen according to screening measurements (if available) and activities' posterior distributions (*pdf*s peaked at zero have been removed). Background Indices prior active background reduction for each detector type have been extracted from parameters posterior distributions for each isotopes/location combination. The values found here are in agreement and even lower with previous estimation made during first part of PhaseII. Most important contributions to BIs are ^{218}Tl and ^{214}Bi located in signal and HV cables for BEGe and semiCoaxial detectors while ^{42}K on n^+ electrode of inverted Coaxial detectors for them.

Bibliography

[1] Fermi, *E. Versuch einer Theorie derβ-Strahlen.* I.Zeitschrift fur Physik88,161–177(Mar. 1934).

[2] Wu, C. S., Ambler, E., Hayward, R. W., Hoppes, D. D. Hudson, R. P. *Experimental Test of Parity Conservation in Beta Decay.* Phys. Rev.105,1413–1415.https://link.aps.org/doi/10.1103/PhysRev.105.1413(4 Feb. 1957).

[3] Goldhaber, M., Grodzins, L. Sunyar, A. *Helicity of neutrinos.* Physical Review109,1015 (1958).

[4] Hamilton, D., Alford, W. Gross, L. *Upper Limits on the Neutrino Mass from theTritium Beta Spectrum.* Physical Review - PHYS REV X92,1521–1525 (Dec. 1953).

[5] Aker, M.et al. *Improved Upper Limit on the Neutrino Mass from a Direct KinematicMethod by KATRIN.* Physical Review Letters123.issn: 1079-7114.http://dx.doi.org/10.1103/PhysRevLett.123.221802(Nov. 2019).

[6] Agostini, M. et al. (GERDA collaboration) *Improved Limit on Neutrinoless Double-β Decay of ^{76}Ge from GERDA Phase II.* Phys. Rev. Lett. 120, 132503. https://link.aps.org/doi/10. 1103/PhysRevLett.120.132503 (13 Mar. 2018).

[7] Fukuda, Y. et al. *Evidence for Oscillation of Atmospheric Neutrinos.* Phys. Rev. Lett. 81, 1562–1567. https://link.aps.org/doi/10.1103/PhysRevLett.81.1562 (8 Aug. 1998).

[8] Ahmad, Q. R. et al. *Measurement of the Rate of $\nu\ e + d \rightarrow p + p + e$ Interactions Produced by ^8B Solar Neutrinos at the Sudbury Neutrino Observatory.* Phys. Rev. Lett. 87, 071301. https://link.aps.org/doi/10.1103/PhysRevLett.87.071301 (7 July 2001).

[9] Goeppert-Mayer, M. *Double Beta-Disintegration.* Phys. Rev. 48, 512–516. https : //link.aps.org/doi/10.1103/PhysRev.48.512 (6 Sept. 1935).

[10] Saakyan, R. *Two-Neutrino Double-Beta Decay.* Annual Review of Nuclear and Particle Science 63, 503–529. eprint: https : / / doi . org / 10 . 1146 / annurev - nucl - 102711 - 094904. https : / / doi . org / 10 . 1146 / annurev - nucl - 102711 - 094904 (2013).

[11] Giunti, C. Kim, C. W. *Fundamentals of Neutrino Physics and Astrophysics* isbn: 978-0-19-850871-7 (Apr. 2007).

[12] Agostini, M. et al. (GERDA collaboration), *The Gerda experiment for the search of $0\nu\beta\beta$ decay in ^{76}Ge.* The European Physical Journal C 73. https://doi.org/10.1140/epjc/s10052-013-2330-0 (2013).

[13] Agostini, M. et al. (GERDA collaboration), *Results on $\beta\beta$ decay with emission of two neutrinos or Majorons in ^{76}Ge from GERDA Phase I.* The European Physical Journal C (Sept. 2015).

[14] Kotila, J. Iachello, F. *Phase-space factors for double-β decay.* Phys. Rev. C 85, 034316. https : / / link . aps . org / doi / 10 . 1103 / PhysRevC . 85 . 034316 (3 Mar. 2012).

[15] Furry, W. H. *On Transition Probabilities in Double Beta-Disintegration.* Phys. Rev. 56, 1184–1193. https://link.aps.org/doi/10.1103/PhysRev.56.1184 (12 Dec. 1939).

[16] Elliott, S. R. Vogel, P. *DOUBLE BETA DECAY.* Annual Review of Nuclear and Particle Science 52, 115–151. eprint: https://doi.org/10.1146/annurev.nucl. 52 . 050102 . 090641. https : / / doi . org / 10 . 1146 / annurev . nucl . 52 . 050102 . 090641 (2002).

[17] Agostini, M. et al. (GERDA Collaboration). *Final Results of GERDA on the Search for Neutrinoless Double-β Decay* 2020. arXiv: 2009.06079 [nucl-ex].

[18] Alvis, S. I. et al. *Search for neutrinoless double-β decay in 76 Ge with 26 kg yr of exposure from the Majorana Demonstrator.* Phys. Rev. C 100, 025501. https:// link.aps.org/doi/10.1103/PhysRevC.100.025501 (2 Aug. 2019).

[19] Andreotti, E. et al. *130Te neutrinoless double-beta decay with CUORICINO.* Astroparticle Physics 34, 822–831. issn: 0927-6505. http://www.sciencedirect.com/ science/article/pii/S0927650511000351 (2011).

[20] Alfonso, K. et al. *Search for Neutrinoless Double-Beta Decay of 130 Te with CUORE-0.* Phys. Rev. Lett. 115, 102502. https://link.aps.org/doi/10.1103/PhysRevLett. 115.102502 (10 Sept. 2015).

[21] Adams, D. Q. et al. *mproved Limit on Neutrinoless Double-Beta Decay in 130 Te with CUORE.* Phys. Rev. Lett. 124, 122501. https : / / link . aps . org / doi / 10 . 1103/PhysRevLett.124.122501 (12 Mar. 2020).

[22] Anton, G. et al. *Search for Neutrinoless Double- Decay with the Complete EXO-200 Dataset.* Phys. Rev. Lett. 123, 161802. https://link.aps.org/doi/10.1103/ PhysRevLett.123.161802 (16 Oct. 2019).

[23] Gando, A. et al. *Search for Majorana Neutrinos Near the Inverted Mass Hierarchy Region with KamLAND-Zen.* Phys. Rev. Lett. 117, 082503. https://link.aps. org/-doi/10.1103/PhysRevLett.117.082503 (8 Aug. 2016).

[24] Dolinski, M. J., Poon, A. W. Rodejohann, W. *Neutrinoless Double-Beta Decay: Status and Prospects.* Annual Review of Nuclear and Particle Science 69, 219–251. eprint: https : / / doi . org / 10 . 1146 / annurev - nucl - 101918 - 023407. https : //doi.org/10.1146/annurev-nucl-101918-023407 (2019).

[25] Gunther, M. et al. *Heidelberg - Moscow beta-beta experiment with Ge-76: Full setup with five detectors.* Phys. Rev. D 55, 54–67 (1997).

[26] Aalseth, C. et al. *Recent results from the IGEX double-beta decay experiment.* Nucl. Phys. B Proc. Suppl. 48 (eds Morales, A., Morales, J. Villar, J.) 223–225 (1996).

[27] Agostini, M. et al. (GERDA collaboration). *Search of Neutrinoless Double Beta Decay with the GERDA Experiment.* Nuclear and Particle Physics Proceedings 273-275. 37th International Conference on High Energy Physics (ICHEP), 1876–1882.

issn: 24056014. http://www.sciencedirect.com/science/article/pii/S2405601415007920 (2016).

[28] Agostini, M. et al. (GERDA collaboration), *Upgrade for Phase II of the Gerda experiment.* Eur. Phys. J. C 78, 388. arXiv: 1711.01452 [physics.ins-det] (2018).

[29] Agostini, M. et al. (GERDA collaboration), *Probing Majorana neutrinos with double-β decay.* Science 365, 1445–1448. issn: 0036-8075. eprint: https : / / science . sciencemag . org / content / 365 / 6460 / 1445 . full . pdf. https : / / science . sciencemag.org/content/365/6460/1445 (2019).

[30] Riboldi, S. et al. *Cryogenic readout techniques for Germanium detectors* 2015 4th International Conference on Advancements in Nuclear Instrumentation Measurement Methods and their Applications (ANIMMA) (2015), 1–6.

[31] Agostini, M. et al. *LArGe - Active background suppression using argon scintillation for the GERDA $0\nu\beta\beta$-experiment 2015.* arXiv: 1501.05762 [physics.ins-det].

[32] Lubashevskiy, A. et al. *Mitigation of 42 Ar/ 42 K background for the GERDA Phase II experiment.* Eur. Phys. J. C 78, 15. arXiv: 1708.00226 [physics.ins-det] (2018).

[33] Freund, K. et al. *The Performance of the Muon Veto of the GERDA Experiment.* Eur. Phys. J. C 76, 298. arXiv: 1601.05935 [physics.ins-det] (2016).

[34] D'Agostini., G. *Bayesian Reasoning In Data Analysis: A Critical Introduction* isbn: 9789814486095. https : / / books . google . sm / books ? id = NqnUCgAAQBAJ (World Scientific Publishing Company, 2003).

[35] Metropolis, N., Rosenbluth, A. W., Rosenbluth, M. N., Teller, A. H., Teller, E. *Equation of State Calculations by Fast Computing Machines*, J. Chem. Phys. 21, 1087 (1953), doi: 10.1063/1.1699114.

[36] Beaujean, F., Caldwell, A., Kollár, D. Kröninger, K. *BAT – The Bayesian Analysis Toolkit.* Journal of Physics: Conference Series 331, 072040. https://doi.org/10. 1088

[37] Brun, R. Rademakers, F. *ROOT: An object oriented data analysis framework.* Nucl. Instrum. Meth. A 389 (eds Werlen, M. Perret-Gallix, D.) 81–86 (1997).

[38] James, F. Roos, M. *Minuit - a system for function minimization and analysis of the parameter errors and correlations.* Computer Physics Communications 10, 343– 367. issn: 0010-4655. http://www.sciencedirect.com/science/article/pii/ 0010465575900399 (1975).

[39] Hahn, T. *Cuba—a library for multidimensional numerical integration.* Computer Physics Communications 168, 78–95. issn: 0010-4655. http://dx.doi.org/10. 1016/j.cpc.2005.01.010 (June 2005).

[40] Agostini, M. et al., *The MGDO software library for data analysis in Ge neutrinoless double-beta decay experiments.* J. Phys. Conf. Ser. 375 (eds Oberauer, L., Raffelt, G. Wagner, R.) 042027. arXiv: 1111.7260 [physics.data-an] (2012).

[41] Agostini, M., Pandola, L., Zavarise, P. Volynets, O. *GELATIO: a general framework for modular digital analysis of high-purity Ge detector signals.* Journal of In- strumentation 6, P08013–P08013. https://doi.org/10.10882F08

[42] Agostini, M., Pandola, L. Zavarise, P. *Off-line data processing and analysis for the GERDA experiment.* Journal of Physics: Conference Series 368, 012047. https:

//doi.org/10.1088$%5C%2F1742 − 6596%5C%2F368%5C%2F1%5C%$2F012047(June 2012).

[43] Agostini, M. et al. (GERDA collaboration), *The background in the* $0\nu\beta\beta$ *experiment* GERDA. Eur. Phys. J. C 74. https://doi.org/10.1140/epjc/s10052- 014- 2764-z (20214).

[44] Agostini, M. et al. (GERDA collaboration).*Modeling of GERDA Phase II data.* J. High Energ. Phys. 139. https://doi.org/10.1007/JHEP03(2020)139 (2020).

[45] Boswell, M. et al. *MaGe-a Geant4-Based Monte Carlo Application Framework for Low-Background Germanium Experiments.* IEEE Transactions on Nuclear Science 58, 1212–1220 (2011).

[46] Agostinelli, S. et al. *GEANT4–a simulation toolkit.* Nucl. Instrum. Meth. A 506, 250–303 (2003).

[47] Allison, J. et al. *Geant4 developments and applications.* IEEE Transactions on Nuclear Science 53, 270–278 (2006).

[48] Allison, J. et al. *Recent developments in Geant4.* Nucl. Instrum. Meth. A 835, 186–225 (2016).

[49] Tretyak, V. I. Zdesenko, Y. G. *TABLES OF DOUBLE BETA DECAY DATA—AN UPDATE.* Atomic Data and Nuclear Data Tables 80, 83–116. issn: 0092-640X. http://www.sciencedirect.com/science/article/pii/S0092640X01908733 (2002).

[50] O.A. Ponkratenko, V. T. Zdesenko., Y. *Event generator DECAY4 for simulating double-beta processes and decays of radioactive nuclei.* Phys. Atom. Nuclei 63, 1282–1287. https://doi.org/10.1134/1.855784 (2000).

[51] Beaujean, F., Caldwell, A., Kollár, D. Kröninger, K. *p-values for model evaluation.* Phys. Rev. D 83, 012004. https://link.aps.org/doi/10.1103/PhysRevD.83. 012004 (1 Jan. 2011).